A Neuroendocrine Modulation to Sustain *C. elegans* Forward Locomotion

Maria A. Lim[1#], Jyothsna Chitturi[1,2], Valeriya Laskova[1,3], Jun Meng[1,3], Daniel Findeis[4], Anne Wiekenberg[4], Ben Mulcahy[1], Linjiao Luo[5], Yan Li[1,3], Yangning Lu[1,3], Wesley Hung[1], Yixin Qu[1], Chi-Yip Ho[1], Douglas Holmyard[1], Rebecca McWhirter[6], Ni Ji[6], Aravinthan D. T. Samuel[6], David M. Miller, III[7], Ralf Schnabel[4], John A. Calarco[8#], Mei Zhen[1,2,3#]

[1] Lunenfeld-Tanenbaum Research Institute, Mount Sinai Hospital, Toronto, ON, Canada

[2] Institute of Medical Science, University of Toronto, Toronto, ON, Canada

[3] Department of Physiology, University of Toronto, Toronto, ON, Canada

[4] Technische Universität Braunschweig Carolo Wilhelmina, Institut für Genetik, Braunschweig, Germany

[5] Key Laboratory of Modern Acoustics, Ministry of Education, Department of Physics, Nanjing University, Nanjing 210093, China

[6] Center for Brain Science and Department of Physics, Harvard University, Cambridge, MA, USA

[7] Department of Cell and Developmental Biology, Vanderbilt University, Nashville, TN, USA

[8] FAS Center for Systems Biology, Harvard University, Cambridge, MA, USA

Correspondence (lim@lunenfeld.ca; jcalarco@fas.harvard.edu; zhen@lunenfeld.ca)

Highlights

- RID is a specialized peptidergic neuron.
- UNC-39/Six/SO governs RID neurogenesis.
- Subtractive RNA profiling uncovers FLP, INS and NLP neuropeptides in RID.
- RID sustains *C. elegans* forward locomotion in part through FLP-14.

Summary

Neuromodulators shape neural circuit dynamics. Combining electron microscopy, genetics, transcriptome profiling, calcium imaging and optogenetics, we discovered a peptidergic neuron that sustains *C. elegans* forward movement. The Six/SO-family homeobox transcription factor UNC-39 governs lineage-specific neurogenesis to give rise to a neuron called RID. RID bears hallmarks of a specialized neuroendocrine: it harbors near-exclusive dense core vesicle clusters along the axon, and expresses multiple neuropeptides, including FLP-14. RID activity increases during forward movement. Ablating RID reduces the sustainability of forward movement, a phenotype partially recapitulated by removing FLP-14. Activating RID prolongs forward movement, an effect that requires FLP-14. In summary, RID is a specialized endocrine neuron that promotes *C. elegans* forward motor state in part through a neuropeptide FLP-14.

Introduction

While classic neurotransmitters activate receptors near their release sites to trigger rapid and short-lived responses, neuromodulators, released by dense core vesicles (DCVs), possess longer half-lives and may diffuse over distances. As such, they can evoke prolonged, as well as long-range responses through metabotropic G-protein-coupled receptors (GPCRs). Neuromodulation exerts profound and lasting effects on animal physiology and behaviors (Hartenstein, 2006; van den Pol, 2012). Its disruption has been associated with pathological states including sleep disorders, metabolic syndromes, and psychiatric disorders (Benarroch, 2013; Sakurai et al., 2010; Sohn et al., 2013). Despite their ancient and fundamental roles, we have limited knowledge on how neuroendocrine cells develop, evolve and function.

Neuroendocrine development and function has been examined in various animal models (Hartenstein, 2006; van den Pol, 2012). The rodent hypothalamus is a well-established hormonal producing and releasing center that controls appetite, reproduction, circadian rhythms, and social behaviors (Graebner et al., 2015; Schwartz et al., 1996; Strauss and Meyer, 1962). Studies in invertebrate models, however, made the key contribution to establishing the fundamental principle that neuromodulators modify properties of neurons and their connections that underlie physiological states and behaviors. Since the discovery of neuromodulators that enable the rhythm-generating crustacean stomatogastric gangalion to produce a multitude of motor patterns for gut movement, various neuromodulators that act on invertebrate circuits to affect movement, aggregation, sleep, arousal, learning and aggregation behaviors have been reported (reviewed in Frooninckx et al., 2012; Marder et al., 2014; Taghert and Nitabach, 2012). Cross-species conservation of neuromodulator function may also be emerging. For example, Pigment Dispersing Factor (PDF), a neuropeptide that couples the motor rhythm with the circadian clock in *Drosophila* (Renn et al., 1999), also couples the motor rhythm with the *C. elegans* developmental clock, cyclic molting (Choi et al., 2013; Li and Kim, 2010; Raizen et al., 2008).

The *C. elegans* model allows for a genetic dissection of the roles and pathways of neuromodulators on behaviors (Frooninckx et al., 2012; Holden-Dye and Walker, 2013; Koelle, 2016). In addition to biogenic amine neuromodulators, its genome contains 113 genes that may

encode up to 250 distinct peptides of three classes (Li and Kim, 2010): the insulin-like (INS) (Pierce et al., 2001), FMRF-amide-related (FLP), and non-insulin/non-FMRF-amide-related (NLP) (Husson et al., 2007). A number of these neuropeptides already have assigned roles, from affecting 'simple' (locomotion, feeding, egg-laying) to 'complex' (mating, lethargus, learning, aggregation) behaviors (Beets et al., 2012; Bendena et al., 2008; Bhattacharya et al., 2014; Chalasani et al., 2007; Chen et al., 2013; Choi et al., 2013; de Bono and Bargmann, 1998; Garrison et al., 2012; Hums et al., 2016; Janssen et al., 2009; Macosko et al., 2009; Tomioka et al., 2006; Turek et al., 2016; Waggoner et al., 2000; others). For instance, the NLP-type PDF-1 increases velocity and suppresses reversals through premotor and other interneurons. An INS-type INS-1 is secreted by an interneuron (AIA) to alter an animal's taxis behavior towards salt upon starvation. NPR-1, a receptor for the FLP-type FLP-18 and FLP-21, mediates context-dependent avoidance and aggregation behavior.

Specialized neuroendocrine systems that modulate animal physiology, neural circuit properties and their outputs through peptidergic signaling have been described in many animals (Hartenstein, 2006; van den Pol, 2012). The morphology and identity of the *C. elegans* neuroendocrine system however remain to be clearly defined and described. Albertson and Thomson (1976) reported the first candidate *C. elegans* secretory neuron (NSM) to contain both clear and dense core vesicles. White et al. (1986) described another neuron (BDU) to 'have striking, darkly staining vesicles'. Reporters for neuropeptide-encoding genes are being found to exhibit expression across the nervous system. Many neuromodulators of known functions act through neurons that clearly participate in classical chemical synaptic transmission. Together, they led to the speculation that all *C. elegans* neurons secrete neuromodulators (Holden-Dye and Walker, 2013), which predicts distributed peptidergic signaling.

However, as noted (White et al., 1986), the EM samples utilized in above anatomic studies were optimized for visualization of presynaptic densities (active zones), not vesicle preservation. This makes unambiguous anatomic determination of neurons with specialized endocrine properties (expected to lack active zones) challenging. Recently, we completed the serial EM reconstruction of several *C. elegans* larvae (unpublished) that were prepared by high-

pressure freezing, which allows for preservation of intracellular structures in physiological states (Rostaing et al., 2004; Weimer, 2006). These and our other EM studies reveal two cohorts of *C. elegans* secretory neurons: one, including NSM, BDU and others, exhibits anatomic properties supporting both neurosecretory and classic synaptic transmission; the other group exhibits predominantly secretory features. RID, a neuron currently of incomplete anatomic reconstruction (White et al., 1986) and unknown function belongs to the latter group.

The survival of animal species depends on their ability to generate appropriate motor responses to a dynamic environment. Like all other animals, *C. elegans* responds to cues from their surroundings by altering motor strategies. How a hard-wired sensorimotor circuit adjusts its output constitutes a central question for neuroscience. Through anatomic, developmental, and functional analyses, we determine that a specialized peptidergic neuron RID modulates the *C. elegans* motor state to favor a sustained forward movement, and it does so in part through secreting a neuropeptide FLP-14. RID serves as a model to probe mechanisms that underlie neuroendocrine development, evolution, and modulation of circuit dynamics.

Results

The RID axon exhibits periodic varicosities that contain near-exclusive DCV clusters devoid of active zones

We reconstructed the dorsal nerve cord (DNC), a fascicle consisting of multiple motor neuron processes that innervate the dorsal body wall muscles. We reconstructed the entire length of a first stage larva (L1), and fragments of multiple young adults, by serial transmission electron microscopy (sTEM) (Figure 1A-C; Supplemental Methods). In all samples, we observed a single process that adopts a stereotypic location in the DNC and exhibits the hallmark features of a specialized neuroendocrine cell. Based on the topology of the fully reconstructed neuron and other criteria (Supplemental Methods), we identified that this process is the axon of a neuron named RID. As described in White et al. (1986), the RID soma resides in the anterior dorsal head ganglion. It sends a ventral-projecting process that reaches the ventral ganglion, loops around to

enter the dorsal ganglion, turns posteriorly to enter the DNC, and runs along the entire length of DNC to reach the tail (illustrated in Figure 1A).

Our L1 and adult DNC reconstruction revealed several unreported features for the RID axon and the DNC. The DNC innervates the dorsal body wall muscles through *en passant* neuromuscular junctions (NMJs) (White et al., 1986). The RID process resides dorsally within the fascicle, nested between the epidermis and GABAergic (DD class) motor neuron processes. It exhibits periodic changes in diameters, from ~40nm to ~ 400nm (L1s) and ~40nm to ~750nm (adults), creating regularly spaced varicosities at ~1.3μm (L1) and ~2.5μm (adult) intervals, along its entire length (Figure 1B, C). These varicosities intercalate between NMJs. In adults, they typically reside immediately posterior to NMJs made by the DD motor neurons (Figure 1C).

The morphological features of these varicosities are distinct from that of their neighboring NMJs (Movie S1). In both L1s and adults, NMJs made by all classes of motor neurons contain a mixed vesicle population with a stereotypic structural organization: a large pool of clear synaptic vesicles adjacent to an active zone (415.6±83.2 per bouton, by adult DD), and a small pool of DCVs residing at the periphery (10.5±2.4 per bouton, by adult DD) (Figure 1C). In contrast, varicosities along the RID axon contain almost exclusively DCVs (20.3±7.8 per bouton, by adult RID axon), the vast majority (78 out of 87) devoid of active zones. A small fraction of varicosities (9 out of 87) contain an active zone-like electron density, but none has associated DCVs.

RID can load and release neuropeptides. Consistent with these EM observations, a fluorescently labeled tyrosine phosphatase receptor IDA-1 (Zahn et al., 2001) marker in RID produced a pearling pattern along the DNC, consistent with periodic DCV accumulation at specific locations along its process (Figure 1D). The exogenous expression of INS-22::GFP, a *C. elegans* neuropeptide marker (Sieburth et al., 2005) in RID resulted in a similar pearling pattern that co-localized with IDA-1::RFP (Figure 1D). INS-22::GFP signals also accumulated in coelomocytes (Figure 1D), the scavenger cells that endocytose secreted substances. Hence RID exhibits the anatomic features of an endocrine cell that predominantly secretes neuropeptides.

UNC-39, the SIX/SO homeobox transcription factor, governs RID neurogenesis

To address the role of RID, we performed a visual screen for genetic mutations that disrupt RID development. Using a fluorescent reporter (*Pceh-10*-GFP, generated based on Altun-Gultekin et al., 2001; Svendsen and McGhee, 1995) that is expressed by four neurons (RID, AIY, CAN, ALA) and a sheath cell, we isolated a mutant *hp701* that exhibits fully penetrant and specific loss of the marker expression in RID (Figure 2A). *hp701* harbors a C to T substitution that results in a recessive and causative missense P298L mutation in *unc-39* (Figure 2B; Methods). A canonical loss-of-function *unc-39* allele *e257,* which harbors a R203Q missense mutation (Yanowitz et al., 2004), fully recapitulates *hp701*'s RID phenotype (Figure 2B) and failed to complement *hp701*.

UNC-39 is a homeobox transcription factor of the SIX/SO family. SIX/SO have been implicated in the development of the eye (Cheyette et al., 1994) and an endocrine gland in *Drosophila* (De Velasco et al., 2004), as well as of the forebrain in several vertebrates (Lagutin et al., 2003). In *C. elegans*, previous studies revealed its role in post-embryonic mesodermal differentiation, as well as the soma or neurite migration, and/or fate marker expression in several other neurons (Manser and Wood, 1990; Yanowitz et al., 2004). As reported (Yanowitz et al., 2004), *unc-39* reporters (Supplemental Methods) were expressed in muscles and multiple neurons from embryos to adults (Figure 2C). Notably, robust expression of *unc-39* reporters was present in the embryonic RID precursor (Figure S1A), embryonic RID (Figure 2C, top panel) and newly hatched L1 larvae (Figure 2C, middle panel). Post-embryonically, *unc-39* expression was specifically decreased in some neurons, including RID (Figure 2C, lower panels).

Our marker analyses, sTEM reconstruction, and embryonic lineage tracing collectively reveal a complete and specific loss of RID terminal differentiation in both *unc-39* alleles. First, all known fate markers (*kal-1*, *ser-2, mod-1, unc-3)* for RID (and other neurons) (Bulow et al., 2002; Tsalik and Hobert, 2003; Wang et al., 2015a) exhibited a complete and specific loss of expression in RID in both *unc-39* alleles (Figure S1B, C). Second, our sTEM reconstruction of segments of the DNCs of several *unc-39* adults failed to reveal a process that morphologically resembles the RID axon (Figure 2E, RID axon denoted in red in wild-type), while all present processes were unambiguously traced back to a motor neuron class (Figure 2E; Supplemental Methods). Third, the lineage development that gives rise to RID (Sulston et al., 1983) exhibited fully penetrant

mitosis and/or terminal differentiation defects in *unc-39* embryos. The ABalappaa neuroblast undergoes two rounds of mitosis: the first produces a posterior daughter, the RID precursor; it divides again and the anterior daughter becomes RID. The sister cells of the RID precursor and RID activate apoptosis shortly after birth (Figure 2D). By simultaneous DIC and fluorescent tracing, we observed that the progeny of ABalappaa followed stereotypic spatial and temporal patterns for mitosis and apoptosis, and its designated anterior granddaughter turned on the *Pceh-10* marker expression shortly after the second mitosis in wild-type embryos (Figure 2D). In *unc-39* embryos, ABalappaa exhibited either a missed, accelerated, or delayed second mitosis, and its progeny did not turn on or maintain the *Pceh-10* marker, and/or, execute apoptosis (Figure 2D).

The anatomic loss of RID in both *unc-39* alleles exhibits striking lineage-specificity. The CAN, ALA, RMED and RIA neurons are lineage-related to RID by sharing progenitors that give rise to ABalappaa (Sulston et al., 1983). These neurons are present in both *unc-39* alleles, with either no or mild and variable defects (e.g. soma position; not shown). RID differentiation thus may be particularly sensitive to the perturbation of UNC-39 activity.

RID synthesizes multiple neuropeptides, including FLP-14 and INS-17

The morphology of RID suggests that it functions as a peptidergic neuron. To identify neuropeptides that are expressed by RID, we performed mRNA sequencing on fully differentiated RID neurons isolated from *C. elegans* larvae. Due to the absence of a strong RID-specific promoter that is required for sorting, we devised a subtractive transcriptome strategy, taking advantage of the specific and complete loss of RID in *unc-39* larvae to detect RID-enriched transcripts. Briefly, we FACS-sorted *Pceh-10*-GFP-positive cells (GFP+ cells) from wild-type and *unc-39(hp701)* second stage larvae (Figure 3A; Supplemental Methods). We compared transcripts of wild-type and *unc-39* GFP+ cells against their respective unsorted whole cell populations (All Cells) (Figure 3B; Supplemental Methods) to obtain two enriched transcript datasets for GFP+ cells in wild-type animals (from RID, ALA, AIY, CAN, and a sheath cell) and *unc-39* mutants (from ALA, AIY, CAN, and a sheath cell). The non-overlapping transcripts

between the two datasets represent candidates that are either differentially expressed in RID, or differentially regulated by UNC-39 (Figure 3C).

Our datasets (Supplemental Methods) were validated using >3 replicates of the wild-type samples. We assessed its quality by two criteria: first, its ability to identify transcripts known to be expressed in RID, ALA, AIY, or CAN (Table 1; Positive Controls). Indeed, we detected significant enrichment for transcripts reported to be expressed by either all GFP+ cells (Svendsen and McGhee, 1995), or a subset of GFP+ cells, e.g. in AIY (*ttx-3*, *hen-1*, *glc-3*, *pdfr-1*) (Flavell et al., 2013; Ishihara et al., 2002; Wenick and Hobert, 2004), and in RID (*lim-4*, *snf-11, zig-5, ser-2* and *kal-1*) (Bulow et al., 2002; Mullen et al., 2006; Tsalik and Hobert, 2003); Second, as importantly, these datasets did not contain transcripts from non-neuronal tissues, such as muscles (*myo-2*, *myo-3),* or, neuronal subtypes not included in GFP+ Cells - the glutamatergic (*eat-4*) and GABAergic (*unc-25*) neurons (Table 1; Negative Controls).

In total, we identified 517 enriched transcripts from wild-type animals, and 800 from *unc-39* mutants (Figure 3C; Table S1). 382 were similarly enriched in both datasets; 555 preferentially enriched in either one of two datasets. Among them, 419 were more enriched in *unc-39* mutant cells, which may represent genes repressed by UNC-39; 136 more enriched in wild-type cells. The last category represents candidates that are either highly enriched in RID, or activated by UNC-39 (Table 1; Table S1). Indeed, among them are *zig-5* and *lim-4*, two known RID markers (Altun-Gultekin et al., 2001; Aurelio et al., 2002; Tsalik and Hobert, 2003).

For the purpose of this study, our follow-up analysis strictly focused on peptide-encoding transcripts. Both wild-type and *unc-39* datasets revealed significant enrichment for a handful of secreted peptide- or protein-encoding transcripts (Figure 3C; Table 1). As expected, those that are similarly enriched in both datasets include peptides known to be expressed by neurons isolated from both wild-type and *unc-39* larvae, e.g. *nlp-15* (AIY) and *hen-1* (CAN, AIY) (Ishihara et al., 2002; Janssen et al., 2009; Nathoo et al., 2001; Wenick and Hobert, 2004). By contrast, *flp-14*, *ins-17* and *nlp-34* showed more enrichment in the wild-type dataset, with *flp-14* and *ins-17* exhibiting the most significant difference, making them candidates highly expressed by RID. Using transcriptional reporters, we confirmed that *flp-14* and *ins-17* are robustly expressed in RID

and additional neurons (Figure 3D, E). For *flp-14*, the other neurons include ALA (not shown), PDE and PLN (Figure 3D), and only tentatively AIM, AIY and AVK (not shown).

RID activity increases during forward locomotion

To address the function of the RID neuron, we monitored its activity pattern in behaving animals by calcium imaging. A genetic calcium sensor GCaMP6, fused with cherry, was expressed by *Pflp-14* to monitor relative neuronal activity change. Parameters for spontaneous locomotion (directionality and instantaneous velocity) and neuronal activity (GCaMP/Cherry) for *Pflp-14* positive neurons were simultaneously acquired as described (Aoyagi et al., 2015; Kawano et al., 2011; Xie et al., 2013; Methods).

RID maintained low activity during reversals, and increased its activity during forward movement (Figure 4A, B). An increased activity was observed in both the RID soma (Figure 4) and axon (Movie S2). No other *Pflp-14*-positive neurons exhibited obvious activity change that correlated with forward movement (Movie S2; not shown). During the transition from reversals to forward movement, we consistently observed an activity rise in RID, typically with a significant lag (~10 seconds) in reaching its peak when compared to the velocity rise (Figure 4A). The RID activity decrease was observed following the transition from forward movement to reversals (Figure 4A, B). There was significant correlation between the rate of velocity change (acceleration and deceleration, X-axis) and of the RID activity change (rise and decay, Y-axis), respectively, when animals transited between forward movement and reversals (Figure 4C; $P<0.006$ for forward to reversal; $P=0.0007$ for reversal to forward movement).

RID sustains forward locomotion

The activation of RID during forward movements, and the positive correlation between the rate of its activity change with that of velocity change during forward and reversal transitions, suggest that RID positively modulates forward movement. To examine this possibility, we quantified the effect of anatomic removal of RID on animals' spontaneous motor behaviors.

C. elegans executes forward movement that is periodically disrupted by pauses, reversals and turns (Gray et al., 2005; Pierce-Shimomura et al., 1999). Our spontaneous motor behavior analyses were performed when wild-type animals exhibit exploratory behaviors (Gao et al., 2015; Supplemental Methods). We quantified the directionality (forward, reversal, pause), speed (instantaneous velocity), and sustainability (duration and frequency of re-initiation of movement from pauses). Under our assay conditions, wild-type *C. elegans* exhibited a predominant preference for forward movement (>95% of total time) over reversals and pauses (<5% combined). RID-ablated animals drastically reduced the propensity for forward movement (~60% of total time), and increased the propensity for reversals (~20%) and pauses (~20%) (Figure 5A). RID-ablated animals exhibited a significant reduction in the duration (Figure 5A') and velocity (Figure S2A) of each forward run, whilst more frequent re-initiation of forward movement (Figure 5A''). They also increased reversal re-initiation frequency (Figure S2A'), without significantly altering reversal duration (Figure S2A"). Hence, upon RID ablation, sustained forward movement was replaced by shorter, slower and frequent forward runs, more pauses and more reversals.

unc-39 mutants, harboring an anatomic loss of RID among other defects, exhibited motor characteristics highly reminiscent to that of the RID-ablated animals – replacing long foraging with more frequent, shorter and slower forward runs, more pauses and more reversals (Figure 5A-A"; Figure S2A-A"; Movie S3 and S4). These behavioral results complement that of the RID calcium imaging, implying not only an association, but also causality of RID activation for sustained foraging.

RID promotes forward movement, in part through FLP-14

We next addressed whether RID's role in sustaining forward runs requires neuropeptides. First, we examined the motor behaviors of *ins-17* and *flp-14* null mutants. *flp-14* mutants exhibited motor characteristics that resembled both *unc-39* and RID-ablated mutants, albeit with reduced severity. Specifically, they also replaced long forward runs with shorter forward bouts, more frequent pauses and reversals (Figure 5A-A"; Figure S2A-A"; Movie S5). Defects in *flp-14*

mutants were less severe than RID ablated or *unc-39* animals: with a less drastic reduction in forward velocity and increase of reversal frequency, they made longer forward runs than *unc-39* mutants and RID-ablated animals (Figure 5A-A"; Figure S2A-A"). A single copy of the wild-type *flp-14* genomic fragment *Si(FLP-14)* reversed the motor defects of *flp-14* mutants (Figure 5B-B"; Figure S2B-B"), confirming the functional requirement of FLP-14 in sustaining forward locomotion. Importantly, in order to determine if FLP-14 from RID contributes to its requirement for sustained forward movement, we removed RID, either by genetic ablation (*unc-39* mutations*)* or laser ablation in the *flp-14; Si(FLP-14)* background. Both resulted in drastically reduced long forward runs (Figure 5B-B", 5C-C" and Figure S2B-B", S2C-C", respectively). By contrast, *ins-17* mutants exhibited motor behaviors undistinguishable from wild-type animals, and *ins-17 flp-14* mutants showed behavioral defects similar to *flp-14* (Figure S2D-D"). These results suggest that RID may be the key cellular origin of FLP-14's role in sustaining forward movement.

In parallel, we addressed this notion by examining the effect of optogenetic activation of RID. Repurposing an endogenous ubiquitin-ligase system (Armenti et al., 2014), we restricted the expression of Chrimson, a light-activated cation channel (Klapoetke et al., 2014) to RID (Supplemental Methods). Stimulating RID using a three-minute light ON/three minute light OFF protocol (Supplemental Methods), we compared the velocity before and after stimulation (Figure 6A, B), and the run length with or without stimulation (Figure 6C). When wild-type animals were executing forward movement, the stimulation of RID induced an ~40% velocity increase (Figure 6A, B; Movie S6). Such a difference was not observed in *unc-39* mutants (Figure 6A, B) and reduced in *flp-14* mutants (Figure 6A, B). Wild-type animals exhibited longer forward runs during periods of light stimulation (Figure 6C). This effect was not observed in either *unc-39* or *flp-14* mutants (Figure 6C). Together, we conclude that RID sustains forward locomotion, with FLP-14 being one of the effectors.

Consistent with the observation that RID activity rise and decay significantly lag behind the directional transition, the optogenetic stimulation of RID when animals were executing reversals did not lead to a prompt switch to foraging (Movie S7). Thus all results consistently point to a modulatory, instead of a deterministic role of RID for the motor state: RID is

dispensable for *C. elegans* to execute or transit between foraging and reversals, but its activation sustains longer forward runs, and such a role requires a neuropeptides LP-14, with additional contribution from unidentified factors.

Discussion

A motor circuit must allow flexibility in its output. This study uncovers a secretory component of the *C. elegans* motor circuit that allows the animal to sustain forward runs. We uncovered the specialized, secretory nature of the RID neuron by sTEM. We identified an RID neurogenetic factor UNC-39 by embryonic lineage tracing. *unc-39* mutants in turn allowed us to identify neuropeptides expressed by RID, FLP-14 and INS-17, among others, by mRNA-sequencing. Combining opto- and behavioral genetics, we revealed that RID sustains forward runs, a role that requires FLP-14 and other effectors. RID hence constitutes part of the circuit mechanism that enables *C. elegans* to adjust the propensity of directional movement.

A multi-layered modulation for *C. elegans'* motor states

Several neuromodulators have been found to enable *C. elegans* to adjust its motor strategy. Some of them function upon modifying the activity of the core motor circuit components that execute the motor patterns. For example, an escape behavior is facilitated by Tyramine released by an interneuron (RIM), which effects the forward-promoting premotor interneuron (AVB) to halt forward movement, and simultaneously, the GABAergic motor neurons (VDs) to induce deep bending (Donnelly et al., 2013; Pirri et al., 2009). Upon exposure to food, dopaminergic sensory neurons activate an NLP-12-releasing interneuron (DVA), which acts upon cholinergic motor neurons (Hu et al., 2011), and reduces forward runs, prompting animals to stay on food (Bhattacharya et al., 2014). Other neuromodulators function through more complex, and less deciphered circuit pathways. For example, PDF-1 promotes forward runs (Janssen et al., 2009) and roaming (Flavell et al., 2013); it is released by the forward-promoting premotor interneuron (AVB) and other neurons, and acts on multiple and upper layer interneurons to promote roaming (Flavell et al., 2013). In response to an oxygen level drop, the NLP-12-releasing interneuron

(DVA) may coordinate with a FLP-1-releasing interneuron (AVK) to facilitate a posture change that is associated with animals halting their forward runs (Hums et al., 2016). Here we uncover a specialized secretory neuron (RID) that promotes the forward runs. The motor circuit appears to be subjected to a multi-layered modulation to enable a flexible and adaptive output.

RID as a modulatory component that sustains forward runs

The core *C. elegans* motor circuit components for executing forward locomotion have been well established: the AVB and PVC premotor interneurons provide electrical and chemical synaptic inputs, respectively, to potentiate the B class cholinergic motor neurons, which innervate and organize muscle contractions in a sequential order to propel the animal forward (reviewed in Zhen and Samuel, 2015, and others). How this core circuit activity is regulated is less clear.

This study identifies a modulator of the output of this basic motor motif. The loss of RID does not abolish the animal's ability to execute forward movement, but reduces its duration and velocity, whilst increasing the propensity for the opposing modes, reversals and pauses. RID exhibits an activity increase after animals switch from reversals to foraging, and a decrease when they transit to reversals. Consistently, in a recent pan-neuronal imaging study, RID was one of the neurons that exhibited a coordinated activity pattern with known components of the forward motor circuit in a fully immobilized animal (Kato et al., 2015). Optogenetic stimulation of RID prolongs forward runs, but is insufficient to cause an immediate switch from the reversal mode to foraging. All results are consistent with RID being a positive modulator for the forward-driving motor circuit.

A full elucidation of the functional connectivity of RID will require extensive future investigation, as our current exploration indicates complexity. Two main inputs to RID are the premotor interneurons of the forward motor circuit, PVC and AVB, in the adult wiring diagram (White et al., 1986). Such a circuit disposition would allow RID to function downstream of the forward-driving premotor interneurons to promote forward bouts. Ablation of PVC and AVB separately (and with other interneurons) did not abolish the RID's activity rise during, or

coordination with, forward movement (Figure S3). They may act redundantly, or with additional inputs to activate RID.

Identifying FLP-14's physiological receptors is necessary for determining RID's downstream signaling. NPR-11 and NPR-4, two GPCRs expressed by several interneurons (Chalasani et al., 2007; Cohen et al., 2009), are the predicted FLP-14 receptors (Frooninckx et al., 2012; Holden-Dye and Walker, 2013). However, in our behavioral assays, *npr-4, npr-11* and *npr-4 npr-11* mutants exhibited either no or very modest locomotory defects when compared to *flp-14* (not shown), and our optogenetic activation of RID in *npr-4 npr-11* mutants yielded identical effect as in wild-type animals (not shown), raising concerns for a simple functional relationship between either receptors and the effect of RID or FLP-14 on forward runs. Because both NPR-4 and NPR-11 have other predicted ligands, it is possible that their effects on forward runs are obscured by the activity of other ligands and neurons that they act upon.

But another possibility, based on studies from the *Ascaris suum*, a parasitic nematode that bears striking similarity in the relevant sensorimotor infrastructure to *C. elegans*, exists. AF2 is the *Ascaris suum* FLP-14. Not only was AF2 expressed by an RID-equivalent neuron (Jarecki et al., 2010), AF2 was capable of potentiating the depolarization of the forward-driven cholinergic motor neurons and body wall muscles upon direct application to the neuromuscular preparation (Cowden and Stretton, 1993; Pang et al., 1995; Trailovic et al., 2005; Verma et al., 2007). A probable anatomic and functional conservation of the FLP-14/AF2 neuropeptide in sustaining forward runs in different nematode species suggests that RID may directly activate body wall muscles and forward-driving motor neurons, and if so, they may act through currently unpredicted receptors.

RID and FLP-14's overlapping and non-overlapping roles

In our behavioral assays, the RID-ablated animals bear close resemblance to the characteristics and severity of the motor defects exhibited by our *unc-39* mutants. In contrast, the RID-less animals and *flp-14* mutants consistently exhibited more obvious difference in severity – the RID-less animals exhibited more drastic reduction of long forward runs and increase of pauses and

reversals (Figure 4; Figure S3). Because the genetic lesion in the *flp-14* allele used in this study removes the entire peptide-coding sequences, such a difference could not be attributed to any residual FLP-14 activity, but rather, indicates that either RID has FLP-14-independent effectors to promote forward runs, and/or, FLP-14 functions at additional neurons that exert an opposing effect on the forward runs.

For the former, we have examined the potential involvement of various candidates. We excluded the likelihood of a major involvement of the other abundantly expressed neuropeptide by RID, INS-17, because *ins-17* mutants did not exhibit motor defects (Figure S2D). NLP-34 could be another RID effector despite its less significant enrichment in RID (Table 1), but a lack of *nlp-34* mutants prevented us from examining its involvement. PDF-1, a neuropeptide with a known effect on forward runs (Janssen et al., 2010), may also be present in RID (Janssen et al., 2010). However, our examination of a PDF-1 reporter strain from a recent study (Sammut et al., 2015) showed that the *Ppdf-1*-positive neuron was instead ALA (not shown); a notion that also explained why in our datasets, *pdf-1* was an equally enriched transcript from both wild-type and *unc-39* animals (Table 1; Figure 3). Lastly, we tested the possibility that defective GABA uptake may also contribute to RID's effect on forward runs, because RID expresses *snf-11*, a plasma membrane GABA transporter (Mullen et al., 2006; and not shown). But *snf-11* mutants did not show changes in forward and reversal propensity, and *snf-11; flp-14* mutants exhibited the same motor characteristics as *flp-14* (not shown). In summary, while we could not examine the involvement of all RID-specific transcripts, we have been unable to identify other effectors from available leads or reagents.

These results keep alive another possibility, that FLP-14 plays roles in neurons that have opposing effects on the motor output, consequently skewing the phenotypic presentation of its RID-dependent function. Indeed, our *Pflp-14* reporter exhibited expression in multiple neurons, some of which have been implicated in promoting pauses (ALA) (Fry et al., 2014; not shown) or inhibiting reversals (AIY) (Gray et al., 2005). Moreover, we have found that an optogenetic, simultaneous activation of all *Pflp-14*-positive neurons induced an immediate transition to reversals, instead of promoting forward runs (not shown).

We propose that while FLP-14 is an effector of RID's role in sustaining forward runs, RID functions through additional effectors, and FLP-14 may play additional roles through neurons that have opposing effects on the motor output from RID. Because most *C. elegans* neurons are shown or predicted to express classic neurotransmitters as well as multiple neuropeptides, and the latter may interact with multiple receptors, an incomplete phenotypic recapitulation upon the perturbation of neurons, neuropeptides that they produce, and receptors that they act upon, may not be uncommon.

A crucial role of the SIX family transcription factor in mitosis, differentiation and endocrine development

The SIX/SO family transcription factors regulate development (Seo et al., 1999). The *Drosophila SO* is essential for development of the entire visual system (Cheyette et al., 1994) and the corpora cardiac (De Velasco et al., 2004). Vertebrate Six3 specifies the embryonic forebrain development as well as its regionalization (Lagutin et al., 2003). Mutations in human Six genes have been associated with breast cancer (Ford et al., 1998), holoprosencephaly (Roessler and Muenke, 1998), branchio-oto-renal syndrome (Hoskins et al., 2008), and Human Myotonic Dystrophy Type 1 (Harris et al., 2000). This study pinpoints the role of a SIX transcription factor in mitosis, a cellular function that may unify and underlie diverse phenotypes in different organisms.

UNC-39 is a multi-tasking transcription factor, expressed by multiple anterior neuronal and mesodermal lineages in developing embryos (Yanowitz et al., 2004). A broad pattern is consistent with *unc-39* mutants exhibiting variable defects in multiple neuronal and mesodermal cells (Manser and Wood, 1990; Yanowitz et al., 2004). However, the RID lineage is particularly sensitive to the perturbation of UNC-39 activity, exhibiting a near complete loss in *unc-39* partial loss-of-function alleles. A key feature of the RID lineage defect was random timing of the second mitosis. Such a phenotype implies a crucial role for UNC-39 in the onset of and exit from the cell cycle that is to be followed by the RID terminal differentiation. Mechanisms that couple cell cycle and terminal differentiation have remained elusive, despite the finding that these processes could be experimentally uncoupled (reviewed in Hardwick and Philpott, 2014). UNC-39 and its RID

lineage-specific partners may be responsible for such a coupling. The absence of corpora cardiac, the insect pituitary in *SO* mutants further entices the speculation of a degree of functional conservation by the SIX transcription factors on endocrine development.

Subtractive RNA profiling to reveal lineage-specifying transcripts

A nervous system consists of neurons of enormous morphological and functional diversity. Obtaining their molecular profile facilitates the exploration of cellular properties that endow their wiring and functional specificity, as well as their evolutionary origins. Methods for cell-type specific transcriptome analysis are being optimized to achieve this goal (Molyneaux et al., 2015; Spencer et al., 2014). Markers that label each single neuronal class are typically required for such analyses, but such markers are often unavailable. This obstacle may be addressed by complementary strategies: double-labeling, improving the efficacy of RNA profiling (Crocker et al., 2016; Klein et al., 2015; Macosko et al., 2009), genetic manipulation to restrict the marker expression, and as presented here, a subtractive transcriptome analysis.

Methods to collect sufficient quantities of fully differentiated neurons from intact *C. elegans* for mRNA sequencing have been developed (Kaletsky et al., 2016; Spencer et al., 2014; Wang et al., 2015b). By comparing the transcriptome profiles obtained from cells harvested from wild-type animals and *unc-39* mutants, we established a robust pipeline that led to the identification of both reported and previously unknown RID transcripts; some are candidate transcripts activated or repressed by UNC-39. The functional validation of FLP-14 by this study suggests that this dataset will be useful for other studies, including identifying potential UNC-39 targets. Animal models such as *C. elegans* and *Drosophila* have a rich repertoire of genetic tools including mutants with specific and known lineage changes (Hobert, 2011). A well-controlled subtractive transcriptome analysis should provide not only cell-type markers, but also transcriptional targets that are regulated by lineage-specifying transcription factors.

Figure Legends

Figure 1. RID is a peptidergic neuron

A. Schematic of the RID neuron. **B.** sTEM reconstruction of RID and motor neurons in a L1 animal. Top panel, Skeletal reconstruction of motor neurons and respective processes in dorsal nerve cord (DNC). Yellow, RID; Green, DD; Light blue, DA; Dark blue, DB. Large swellings of the RID neurite are indicated by spheres. Bottom panel, Volumetric reconstruction of the L1 RID cell body and dorsal cord neurite. **C.** Volumetric reconstruction of a portion of the RID axon in a young adult. Bottom: The neurite of RID (yellow), DD (pink). Middle: higher magnification versions of the regions indicated by the dashed boxes i, ii and iii. Top: Representative EM cross-section images of RID and DD boutons in the adult DNC. In the volumetric reconstruction, green spheres indicate SVs, blue spheres DCVs, red shading indicates active zones, and light blue shading indicates mitochondria. **D.** Top panels, a cytoplasmic GFP reporter illustrates the RID axon, followed by reporters for the DCV membrane protein IDA-1 and the neuropeptide INS-22 along the RID axon. Bottom panel, INS-22::GFP accumulated at coelomocytes (dotted circle), indicating that it was secreted. Scale bar, 5 μm.

Figure 2. RID fails to differentiate in *unc-39* mutants

A. In *unc-39* mutants, RID soma (circle) and axon could not be detected by the *Pceh*-10-GFP marker, while *Pceh-10*-GFP cells are present. Scale bar, 10 μm. **B.** A predicted protein structure of UNC-39 compared with its Drosophila homologue SO, denoted with allelic information of *hp701* and *e257* mutations. **C.** *unc-39* expression in the nervous system was observed in embryos (top panel), newly hatched L1 larvae (middle panel), and young adults (lower two panels). Scale bar, 10 μm.**D.** Lineage map of ABalappaa, the neuroblast that gives rise to RID (ABalappaa**pa**) in embryos of wild-type animals and *unc-39* mutants. *unc-39* mutants exhibited a range of mitosis changes. **E.** Skeletal sTEM reconstruction of a fragment of the DNC of a wild-type and *unc-39* mutant. The RID axon is absent from the *unc-39* DNC. Red, RID; Yellow, DD; Green, VD; Light blue, DA/AS; Dark blue, DB. **F.** Representative images of the EM cross-section from the DNC of *unc-39* mutants. Numbers (1-3) denote their approximate locations in **E.** RID process is absent in

all three sections. The identity of neurons, hypodermis and muscles are labeled accordingly. Scale bar, 500 nm.

Figure 3. Subtractive transcriptome profiling reveals neuropeptides expressed by RID

A. The Experimental design and schematic of cell isolation protocol by flow cytometry. SSC, side scatter. **B.** The workflow of data analysis. **C.** A venn diagram representation of neuropeptide transcripts enriched in wild-type and *unc-39* datasets. **D.** A transcriptional reporter of *Pflp-14* exhibits expression in RID cell body (circle), along the RID axon (arrowheads) and other neurons, including those in the mid-body (PDE, bottom left panel) and tail (PLN, bottom right panel). Scale bar, 10 μm. **E.** A transcriptional reporter of *Pins-17* exhibits expression in RID (circle) and other unidentified neurons. Scale bar, 10 μm. **F.** Scale bar, 10 μm.

Figure 4. RID activity increase correlates with forward movements

A. Representative velocity (top) and corresponding RID calcium activity trace (bottom) from a freely moving animal. Normalized ratiometric signal changes (ΔF/F), as well as the raw fluorescence intensities of GCaMP and cherry are shown. ΔF/F was used to calculate changes in calcium activity for each animal. Changes in positions of fluorescent signals were used to calculate velocity and directionality. **B**. RID activity as measured by GCaMP/cherry ratio change (± SEM) during transition periods. **Left panel,** RID activity increases when animals transition from backward to fast forward locomotion. **Right panel**, RID activity decreases when animals transition from forward to backward locomotion. For **A** and **B**, dotted longitudinal lines indicate transition period from backward to forward locomotion and vice versa. **C.** Cross-correlation analyses between the change in RID activity and the change in velocity. Positive and negative slopes (Y-axis) indicate increase and decrease in RID activity, respectively. Positive and negative values on the X-axis indicate changes in velocity from backward to forward locomotion (acceleration) and from forward to backward locomotion (deceleration), respectively. For **B** and **C**, n=10, each dot represents a transitional event.

Figure 5. RID and FLP-14 potentiate sustained, long forward movements

A-A". Spontaneous motor behavioral output, the propensity of directional movement (A) and the continuity of forward movement (A' and A"), between wild-type control (mock-ablated *Pceh-10*-GFP *animals*), RID-ablated *Pceh-10*-GFP animals, wild-type (N2), *unc-39,* and *flp-14* mutants. They decreased the propensity for long forward runs, replacing it with more frequent reversals and pauses. A) Total fractional time animals of each genotype spent in forward, reversal, or pauses; A') Duration of forward runs; and A") Frequency of re-initiation of forward runs. RID-ablated, *unc-39* and *flp-14* animals exhibit decreased duration of forward bouts and increased frequency of re-initiation of forward bouts from wild-type control. **B-B".** Spontaneous motor output of wild-type control (Si(FLP-14) animals), *flp-14, flp-14;Si (FLP-14),* and *flp-14;unc-39;Si (FLP-14)* animals. A single copy of FLP-14 reversed *flp-14* mutants' motor defects, but not in the *unc-39* background. **C-C".** Spontaneous motor output of wild-type control (Si(FLP-14) animals), *flp-14*, *flp-14;Si(FLP-14)* and *flp-14;Si(FLP-14) RID ablated animals*. A single copy of FLP-14 reversed *flp-14* mutants' motor defects, an effect abolished when RID was laser ablated.

Figure 6. Activation of RID promotes forward movements in part through FLP-14

A-B. A comparison of the motor behavior response before and after RID optogenetic stimulation in wild-type, *unc-39* and *flp-14* animals. The change of speed (phasic velocity) before and after RID stimulation (Lights ON) in wild-type, *unc-39* and *flp-14* animals, respectively, was quantified in B. **C.** The distribution of the mean run length for all light ON (RID stimulation) and light OFF (no RID stimulation) periods. An increase of velocity and run length in response to RID stimulation was observed in wild-type, abolished in *unc-39* mutants, and reduced in *flp-14* mutants.

Experimental Procedures

Strains and constructs

C. elegans were cultured on standard Nematode Growth Medium (NGM) plates seeded with OP50, and maintained at 22°C. *hp701* was isolated by EMS mutagenesis of a strain carrying an integrated *Pceh-10-GFP* array (*hpIs202*), identified through a combination of SNP mapping and whole genome sequencing (Davis and Hammarlund, 2006; Doitsidou et al., 2010), followed by rescuing by a *unc-39*-containing fosmid and a *unc-39* minimal genomic clone. *hp701* and other mutants obtained from the *Caenorhabditis* Genetics Center (CGC) were backcrossed at least 4x against N2 prior to usage. See Supplemental Information for a complete list of mutants, transgenic lines, and constructs.

Electron Microscopy

L1 (N2) or young adult animals (N2 and *hp701*) were packed into 3mm diameter aluminum carriers and frozen using a Leica EM HP100 high-pressure freezer. Subsequent fixation and freeze substitution was performed as described (Weimer, 2006). Samples were infiltrated and embedded in the Spurr resin. 70 nm transverse serial sections were prepared and imaged using the FEI Techai 20 TEM at 200 kV (x29,000). For L1, the entire length of RID axon along the dorsal cord was reconstructed. For adults, 20-30 μm of the dorsal nerve cord was reconstructed. See Supplemental Information on EM reconstruction and analyses.

Embryonic Lineage Analysis

Strains (*hpIs202* and *unc-39; hpIs202*) were cultured and recorded at 25°C. Embryos were mounted at 1-4 cell stages, and recorded every 35 sec with 25 z-levels. After ~350 z-scans (200 min) with DIC optics, the GFP fluorescence optics was automatically activated and exposed for every 20th z-scan till 320 min of development, and then every 30th z-scan till the 3-fold stage. Recording was performed at 630x on a 4D microscope controlled by *TimeToLive* (*Caenotec*-Prof. Ralf Schnabel r.schnabel@tu-bs.de). RID and neighboring lineage cells were traced using

SIMI°Biocell (SIMI Reality Motion Systems GmbH, http://www.simi.com/de/home.html) until the late 1.5-fold stage (340 and 360 min) as described (Schnabel et al., 1997).

Preparation of Dissociated Larval Cells for Cell Sorting

Synchronized *hpIs202 (Pceh-10-GFP)* and *unc-39(hp701); hpIs202* larval stage 1 (L1) animals were grown on 150 mm 8P plates seeded with NA22 for approximately ~12 hours until they reached larval stage 2 (L2). Cells were extracted from L2s. See Supplemental Information for methods.

Laser Ablation

Synchronized *hpIs202 (Pceh-10-GFP)* L1 animals were immobilized and RID ablated using the MicroPoint laser as described (Fang-Yen et al., 2012). Mock-ablated animals were L1s of the same genotype processed similarly, except that they were not exposed to the laser. L4 RID- and mock-ablated animals were confirmed for the status of RID prior to locomotion analyses.

Locomotion Assay

Automated tracking and locomotion analyses were performed as described (Gao et al., 2015). Detailed description of experimental conditions is provided in the Supplemental Information.

Calcium imaging

The third stage (L3) *hpIs587 (Pflp-14-GCaMP6::cherry)* animals were placed on a drop of M9 buffer on top of a 2.5% agar pad, covered with a cover slip. Four ~1 mm x 1 mm 0.001 inch-thick polycarbonate pieces (Catalog # 9513K12, McMaster-Carr) between the agar pad and coverslip served as spacers to allow movement. Each recording lasted for 3 minutes. Images were captured using a 20x objective on a Zeiss Axioskop 2 Plus equipped with an ASI MS-40000 motorized stage, a dual-view beam splitter (Photometrics) and a CCD camera (Hamamatsu Orca-R2). The 4x-binned images were obtained at 10 frames per second. See Supplemental Information for detailed methods.

Optogenetic stimulation

We restricted the expression of a codon-optimized version of Chrimson to the RID neuron, and stimulated wild-type, *flp-14(gk1055)* and *unc-39(hp701)* animals carrying the same transgene using a Diode red laser while animal locomotion was tracked under dark-field imaging by infrared light. The stimulation and tracking were performed using the Colbert (COntrol Locomotion and BEhavior in Real Time) system (Leifer et al., 2011). The locomotion was recorded for each animals, and their trajectories were then extracted and analyzed as described analyzed as previously described (Luo et al., 2014). See Supplemental Information for detailed methods.

Author Contributions

MZ and WH conceived the study; all authors designed and performed experiments or analyses; MAL, JAC and MZ wrote the manuscript; all authors edited or approved the manuscript.

Acknowledgements

We thank D. Witvliet, Y. Wang and Q. Jin for technical assistance and EM analysis; *CGC*, H. Hutter and O. Hobert for strains, D. Moerman and S. Flibotte for whole-genome sequencing analyses. This work is supported by CIHR and NSERC (to MZ) and NIH (to JAC).

References

Albertson, D.G., and Thomson, J.N. (1976). The pharynx of Caenorhabditis elegans. Philosophical transactions of the Royal Society of London Series B, Biological sciences *275*, 299-325.

Altun-Gultekin, Z., Andachi, Y., Tsalik, E.L., Pilgrim, D., Kohara, Y., and Hobert, O. (2001). A regulatory cascade of three homeobox genes, ceh-10, ttx-3 and ceh-23, controls cell fate specification of a defined interneuron class in C. elegans. Development *128*, 1951-1969.

Aoyagi, K., Rossignol, E., Hamdan, F.F., Mulcahy, B., Xie, L., Nagamatsu, S., Rouleau, G.A., Zhen, M., and Michaud, J.L. (2015). A Gain-of-Function Mutation in NALCN in a Child with Intellectual Disability, Ataxia, and Arthrogryposis. Hum Mutat *36*, 753-757.

Armenti, S.T., Lohmer, L.L., Sherwood, D.R., and Nance, J. (2014). Repurposing an endogenous degradation system for rapid and targeted depletion of C. elegans proteins. Development *141*, 4640-4647.

Aurelio, O., Hall, D.H., and Hobert, O. (2002). Immunoglobulin-domain proteins required for maintenance of ventral nerve cord organization. Science *295*, 686-690.

Beets, I., Janssen, T., Meelkop, E., Temmerman, L., Suetens, N., Rademakers, S., Jansen, G., and Schoofs, L. (2012). Vasopressin/oxytocin-related signaling regulates gustatory associative learning in C. elegans. Science *338*, 543-545.

Benarroch, E.E. (2013). Oxytocin and vasopressin: social neuropeptides with complex neuromodulatory functions. Neurology *80*, 1521-1528.

Bendena, W.G., Boudreau, J.R., Papanicolaou, T., Maltby, M., Tobe, S.S., and Chin-Sang, I.D. (2008). A Caenorhabditis elegans allatostatin/galanin-like receptor NPR-9 inhibits local search behavior in response to feeding cues. Proceedings of the National Academy of Sciences of the United States of America *105*, 1339-1342.

Bhattacharya, R., Touroutine, D., Barbagallo, B., Climer, J., Lambert, C.M., Clark, C.M., Alkema, M.J., and Francis, M.M. (2014). A conserved dopamine-cholecystokinin signaling pathway shapes context-dependent Caenorhabditis elegans behavior. PLoS genetics *10*, e1004584.

Bulow, H.E., Berry, K.L., Topper, L.H., Peles, E., and Hobert, O. (2002). Heparan sulfate proteoglycan-dependent induction of axon branching and axon misrouting by the Kallmann syndrome gene kal-1. Proceedings of the National Academy of Sciences of the United States of America *99*, 6346-6351.

Chalasani, S.H., Chronis, N., Tsunozaki, M., Gray, J.M., Ramot, D., Goodman, M.B., and Bargmann, C.I. (2007). Dissecting a circuit for olfactory behaviour in Caenorhabditis elegans. Nature *450*, 63-70.

Chen, Z., Hendricks, M., Cornils, A., Maier, W., Alcedo, J., and Zhang, Y. (2013). Two insulin-like peptides antagonistically regulate aversive olfactory learning in C. elegans. Neuron *77*, 572-585.

Cheyette, B.N., Green, P.J., Martin, K., Garren, H., Hartenstein, V., and Zipursky, S.L. (1994). The Drosophila sine oculis locus encodes a homeodomain-containing protein required for the development of the entire visual system. Neuron *12*, 977-996.

Choi, S., Chatzigeorgiou, M., Taylor, K.P., Schafer, W.R., and Kaplan, J.M. (2013). Analysis of NPR-1 reveals a circuit mechanism for behavioral quiescence in C. elegans. Neuron *78*, 869-880.

Cohen, M., Reale, V., Olofsson, B., Knights, A., Evans, P., and de Bono, M. (2009). Coordinated regulation of foraging and metabolism in C. elegans by RFamide neuropeptide signaling. Cell Metab *9*, 375-385.

Cowden, C., and Stretton, A.O. (1993). AF2, an Ascaris neuropeptide: isolation, sequence, and bioactivity. Peptides *14*, 423-430.

Crocker, A., Guan, X.J., Murphy, C.T., and Murthy, M. (2016). Cell-Type-Specific Transcriptome Analysis in the Drosophila Mushroom Body Reveals Memory-Related Changes in Gene Expression. Cell Rep *15*, 1580-1596.

Davis, M.W., and Hammarlund, M. (2006). Single-nucleotide polymorphism mapping. Methods in molecular biology *351*, 75-92.

de Bono, M., and Bargmann, C.I. (1998). Natural variation in a neuropeptide Y receptor homolog modifies social behavior and food response in C. elegans. Cell *94*, 679-689.

De Velasco, B., Shen, J., Go, S., and Hartenstein, V. (2004). Embryonic development of the Drosophila corpus cardiacum, a neuroendocrine gland with similarity to the vertebrate pituitary, is controlled by sine oculis and glass. Developmental biology *274*, 280-294.

Doitsidou, M., Poole, R.J., Sarin, S., Bigelow, H., and Hobert, O. (2010). C. elegans mutant identification with a one-step whole-genome-sequencing and SNP mapping strategy. PloS one *5*, e15435.

Donnelly, J.L., Clark, C.M., Leifer, A.M., Pirri, J.K., Haburcak, M., Francis, M.M., Samuel, A.D., and Alkema, M.J. (2013). Monoaminergic orchestration of motor programs in a complex C. elegans behavior. PLoS biology *11*, e1001529.

Fang-Yen, C., Gabel, C.V., Samuel, A.D., Bargmann, C.I., and Avery, L. (2012). Laser microsurgery in Caenorhabditis elegans. Methods in cell biology *107*, 177-206.

Flavell, S.W., Pokala, N., Macosko, E.Z., Albrecht, D.R., Larsch, J., and Bargmann, C.I. (2013). Serotonin and the neuropeptide PDF initiate and extend opposing behavioral states in C. elegans. Cell *154*, 1023-1035.

Ford, H.L., Kabingu, E.N., Bump, E.A., Mutter, G.L., and Pardee, A.B. (1998). Abrogation of the G2 cell cycle checkpoint associated with overexpression of HSIX1: a possible mechanism of breast carcinogenesis. Proceedings of the National Academy of Sciences of the United States of America *95*, 12608-12613.

Frooninckx, L., Van Rompay, L., Temmerman, L., Van Sinay, E., Beets, I., Janssen, T., Husson, S.J., and Schoofs, L. (2012). Neuropeptide GPCRs in C. elegans. Front Endocrinol (Lausanne) *3*, 167.

Fry, A.L., Laboy, J.T., and Norman, K.R. (2014). VAV-1 acts in a single interneuron to inhibit motor circuit activity in Caenorhabditis elegans. Nature communications *5*, 5579.

Gao, S., Xie, L., Kawano, T., Po, M.D., Pirri, J.K., Guan, S., Alkema, M.J., and Zhen, M. (2015). The NCA sodium leak channel is required for persistent motor circuit activity that sustains locomotion. Nature communications *6*, 6323.

Garrison, J.L., Macosko, E.Z., Bernstein, S., Pokala, N., Albrecht, D.R., and Bargmann, C.I. (2012). Oxytocin/vasopressin-related peptides have an ancient role in reproductive behavior. Science *338*, 540-543.

Graebner, A.K., Iyer, M., and Carter, M.E. (2015). Understanding how discrete populations of hypothalamic neurons orchestrate complicated behavioral states. Front Syst Neurosci *9*, 111.

Gray, J.M., Hill, J.J., and Bargmann, C.I. (2005). A circuit for navigation in Caenorhabditis elegans. Proceedings of the National Academy of Sciences of the United States of America *102*, 3184-3191.

Hardwick, L.J., and Philpott, A. (2014). Nervous decision-making: to divide or differentiate. Trends in genetics : TIG *30*, 254-261.

Harris, S.E., Winchester, C.L., and Johnson, K.J. (2000). Functional analysis of the homeodomain protein SIX5. Nucleic acids research *28*, 1871-1878.

Hartenstein, V. (2006). The neuroendocrine system of invertebrates: a developmental and evolutionary perspective. J Endocrinol *190*, 555-570.

Hobert, O. (2011). Regulation of terminal differentiation programs in the nervous system. Annual review of cell and developmental biology *27*, 681-696.

Holden-Dye, L., and Walker, R.J. (2013). The roles of neuropeptides in Caenorhabditis elegans including their importance in the regulation of feeding and metabolism. Protein Pept Lett *20*, 636-646.

Hoskins, B.E., Cramer, C.H., 2nd, Tasic, V., Kehinde, E.O., Ashraf, S., Bogdanovic, R., Hoefele, J., Pohl, M., and Hildebrandt, F. (2008). Missense mutations in EYA1 and TCF2 are a rare cause of urinary tract malformations. Nephrol Dial Transplant *23*, 777-779.

Hu, Z., Pym, E.C., Babu, K., Vashlishan Murray, A.B., and Kaplan, J.M. (2011). A neuropeptide-mediated stretch response links muscle contraction to changes in neurotransmitter release. Neuron *71*, 92-102.

Hums, I., Riedl, J., Mende, F., Kato, S., Kaplan, H.S., Latham, R., Sonntag, M., Traunmuller, L., and Zimmer, M. (2016). Regulation of two motor patterns enables the gradual adjustment of locomotion strategy in Caenorhabditis elegans. Elife *5*.

Husson, S.J., Mertens, I., Janssen, T., Lindemans, M., and Schoofs, L. (2007). Neuropeptidergic signaling in the nematode Caenorhabditis elegans. Prog Neurobiol *82*, 33-55.

Ishihara, T., Iino, Y., Mohri, A., Mori, I., Gengyo-Ando, K., Mitani, S., and Katsura, I. (2002). HEN-1, a secretory protein with an LDL receptor motif, regulates sensory integration and learning in Caenorhabditis elegans. Cell *109*, 639-649.

Janssen, T., Husson, S.J., Meelkop, E., Temmerman, L., Lindemans, M., Verstraelen, K., Rademakers, S., Mertens, I., Nitabach, M., Jansen, G.*, et al.* (2009). Discovery and characterization of a conserved pigment dispersing factor-like neuropeptide pathway in Caenorhabditis elegans. J Neurochem *111*, 228-241.

Janssen, T., Lindemans, M., Meelkop, E., Temmerman, L., and Schoofs, L. (2010). Coevolution of neuropeptidergic signaling systems: from worm to man. Ann N Y Acad Sci *1200*, 1-14.

Jarecki, J.L., Andersen, K., Konop, C.J., Knickelbine, J.J., Vestling, M.M., and Stretton, A.O. (2010). Mapping neuropeptide expression by mass spectrometry in single dissected identified neurons from the dorsal ganglion of the nematode Ascaris suum. ACS Chem Neurosci *1*, 505-519.

Kaletsky, R., Lakhina, V., Arey, R., Williams, A., Landis, J., Ashraf, J., and Murphy, C.T. (2016). The C. elegans adult neuronal IIS/FOXO transcriptome reveals adult phenotype regulators. Nature *529*, 92-96.

Kato, S., Kaplan, H.S., Schrodel, T., Skora, S., Lindsay, T.H., Yemini, E., Lockery, S., and Zimmer, M. (2015). Global Brain Dynamics Embed the Motor Command Sequence of Caenorhabditis elegans. Cell *163*, 656-669.

Kawano, T., Po, M.D., Gao, S., Leung, G., Ryu, W.S., and Zhen, M. (2011). An imbalancing act: gap junctions reduce the backward motor circuit activity to bias C. elegans for forward locomotion. Neuron *72*, 572-586.

Klapoetke, N.C., Murata, Y., Kim, S.S., Pulver, S.R., Birdsey-Benson, A., Cho, Y.K., Morimoto, T.K., Chuong, A.S., Carpenter, E.J., Tian, Z.*, et al.* (2014). Independent optical excitation of distinct neural populations. Nat Methods *11*, 338-346.

Klein, A.M., Mazutis, L., Akartuna, I., Tallapragada, N., Veres, A., Li, V., Peshkin, L., Weitz, D.A., and Kirschner, M.W. (2015). Droplet barcoding for single-cell transcriptomics applied to embryonic stem cells. Cell *161*, 1187-1201.

Koelle, M.R. (2016). Neurotransmitter signaling through heterotrimeric G proteins: insights from studies in C. elegans. WormBook, 1-78.

Lagutin, O.V., Zhu, C.C., Kobayashi, D., Topczewski, J., Shimamura, K., Puelles, L., Russell, H.R., McKinnon, P.J., Solnica-Krezel, L., and Oliver, G. (2003). Six3 repression of Wnt signaling in the anterior neuroectoderm is essential for vertebrate forebrain development. Genes Dev *17*, 368-379.

Leifer, A.M., Fang-Yen, C., Gershow, M., Alkema, M.J., and Samuel, A.D. (2011). Optogenetic manipulation of neural activity in freely moving Caenorhabditis elegans. Nat Methods *8*, 147-152.

Li, C., and Kim, K. (2010). Neuropeptide gene families in Caenorhabditis elegans. Adv Exp Med Biol *692*, 98-137.

Luo, L., Wen, Q., Ren, J., Hendricks, M., Gershow, M., Qin, Y., Greenwood, J., Soucy, E.R., Klein, M., Smith-Parker, H.K.*, et al.* (2014). Dynamic encoding of perception, memory, and movement in a C. elegans chemotaxis circuit. Neuron *82*, 1115-1128.

Macosko, E.Z., Pokala, N., Feinberg, E.H., Chalasani, S.H., Butcher, R.A., Clardy, J., and Bargmann, C.I. (2009). A hub-and-spoke circuit drives pheromone attraction and social behaviour in C. elegans. Nature *458*, 1171-1175.

Manser, J., and Wood, W.B. (1990). Mutations affecting embryonic cell migrations in Caenorhabditis elegans. Developmental genetics *11*, 49-64.

Marder, E., O'Leary, T., and Shruti, S. (2014). Neuromodulation of circuits with variable parameters: single neurons and small circuits reveal principles of state-dependent and robust neuromodulation. Annu Rev Neurosci *37*, 329-346.

Molyneaux, B.J., Goff, L.A., Brettler, A.C., Chen, H.H., Brown, J.R., Hrvatin, S., Rinn, J.L., and Arlotta, P. (2015). DeCoN: genome-wide analysis of in vivo transcriptional dynamics during pyramidal neuron fate selection in neocortex. Neuron *85*, 275-288.

Mullen, G.P., Mathews, E.A., Saxena, P., Fields, S.D., McManus, J.R., Moulder, G., Barstead, R.J., Quick, M.W., and Rand, J.B. (2006). The Caenorhabditis elegans snf-11 gene encodes a

sodium-dependent GABA transporter required for clearance of synaptic GABA. Molecular biology of the cell *17*, 3021-3030.

Nathoo, A.N., Moeller, R.A., Westlund, B.A., and Hart, A.C. (2001). Identification of neuropeptide-like protein gene families in Caenorhabditiselegans and other species. Proceedings of the National Academy of Sciences of the United States of America *98*, 14000-14005.

Pang, F.Y., Mason, J., Holden-Dye, L., Franks, C.J., Williams, R.G., and Walker, R.J. (1995). The effects of the nematode peptide, KHEYLRFamide (AF2), on the somatic musculature of the parasitic nematode Ascaris suum. Parasitology *110 (Pt 3)*, 353-362.

Pierce, S.B., Costa, M., Wisotzkey, R., Devadhar, S., Homburger, S.A., Buchman, A.R., Ferguson, K.C., Heller, J., Platt, D.M., Pasquinelli, A.A.*, et al.* (2001). Regulation of DAF-2 receptor signaling by human insulin and ins-1, a member of the unusually large and diverse C. elegans insulin gene family. Genes Dev *15*, 672-686.

Pierce-Shimomura, J.T., Morse, T.M., and Lockery, S.R. (1999). The fundamental role of pirouettes in Caenorhabditis elegans chemotaxis. The Journal of neuroscience : the official journal of the Society for Neuroscience *19*, 9557-9569.

Pirri, J.K., McPherson, A.D., Donnelly, J.L., Francis, M.M., and Alkema, M.J. (2009). A tyramine-gated chloride channel coordinates distinct motor programs of a Caenorhabditis elegans escape response. Neuron *62*, 526-538.

Raizen, D.M., Zimmerman, J.E., Maycock, M.H., Ta, U.D., You, Y.J., Sundaram, M.V., and Pack, A.I. (2008). Lethargus is a Caenorhabditis elegans sleep-like state. Nature *451*, 569-572.

Renn, S.C., Park, J.H., Rosbash, M., Hall, J.C., and Taghert, P.H. (1999). A pdf neuropeptide gene mutation and ablation of PDF neurons each cause severe abnormalities of behavioral circadian rhythms in Drosophila. Cell *99*, 791-802.

Roessler, E., and Muenke, M. (1998). Holoprosencephaly: a paradigm for the complex genetics of brain development. J Inherit Metab Dis *21*, 481-497.

Rostaing, P., Weimer, R.M., Jorgensen, E.M., Triller, A., and Bessereau, J.L. (2004). Preservation of immunoreactivity and fine structure of adult C. elegans tissues using high-pressure freezing. The journal of histochemistry and cytochemistry : official journal of the Histochemistry Society *52*, 1-12.

Sakurai, T., Mieda, M., and Tsujino, N. (2010). The orexin system: roles in sleep/wake regulation. Ann N Y Acad Sci *1200*, 149-161.

Sammut, M., Cook, S.J., Nguyen, K.C., Felton, T., Hall, D.H., Emmons, S.W., Poole, R.J., and Barrios, A. (2015). Glia-derived neurons are required for sex-specific learning in C. elegans. Nature *526*, 385-390.

Schnabel, R., Hutter, H., Moerman, D., and Schnabel, H. (1997). Assessing normal embryogenesis in Caenorhabditis elegans using a 4D microscope: variability of development and regional specification. Developmental biology *184*, 234-265.

Schwartz, M.W., Seeley, R.J., Campfield, L.A., Burn, P., and Baskin, D.G. (1996). Identification of targets of leptin action in rat hypothalamus. The Journal of clinical investigation *98*, 1101-1106.

Seo, H.C., Curtiss, J., Mlodzik, M., and Fjose, A. (1999). Six class homeobox genes in drosophila belong to three distinct families and are involved in head development. Mech Dev *83*, 127-139.

Sieburth, D., Ch'ng, Q., Dybbs, M., Tavazoie, M., Kennedy, S., Wang, D., Dupuy, D., Rual, J.F., Hill, D.E., Vidal, M.*, et al.* (2005). Systematic analysis of genes required for synapse structure and function. Nature *436*, 510-517.

Sohn, J.W., Elmquist, J.K., and Williams, K.W. (2013). Neuronal circuits that regulate feeding behavior and metabolism. Trends Neurosci *36*, 504-512.

Spencer, W.C., McWhirter, R., Miller, T., Strasbourger, P., Thompson, O., Hillier, L.W., Waterston, R.H., and Miller, D.M., 3rd (2014). Isolation of specific neurons from C. elegans larvae for gene expression profiling. PloS one *9*, e112102.

Strauss, W.F., and Meyer, R.K. (1962). Neural timing of ovulation in immature rats treated with gonadotrophin. Science *137*, 860-861.

Sulston, J.E., Schierenberg, E., White, J.G., and Thomson, J.N. (1983). The embryonic cell lineage of the nematode Caenorhabditis elegans. Developmental biology *100*, 64-119.

Svendsen, P.C., and McGhee, J.D. (1995). The C. elegans neuronally expressed homeobox gene ceh-10 is closely related to genes expressed in the vertebrate eye. Development *121*, 1253-1262.

Taghert, P.H., and Nitabach, M.N. (2012). Peptide neuromodulation in invertebrate model systems. Neuron *76*, 82-97.

Tomioka, M., Adachi, T., Suzuki, H., Kunitomo, H., Schafer, W.R., and Iino, Y. (2006). The insulin/PI 3-kinase pathway regulates salt chemotaxis learning in Caenorhabditis elegans. Neuron *51*, 613-625.

Trailovic, S.M., Clark, C.L., Robertson, A.P., and Martin, R.J. (2005). Brief application of AF2 produces long lasting potentiation of nAChR responses in Ascaris suum. Mol Biochem Parasitol *139*, 51-64.

Tsalik, E.L., and Hobert, O. (2003). Functional mapping of neurons that control locomotory behavior in Caenorhabditis elegans. J Neurobiol *56*, 178-197.

Turek, M., Besseling, J., Spies, J.P., Konig, S., and Bringmann, H. (2016). Sleep-active neuron specification and sleep induction require FLP-11 neuropeptides to systemically induce sleep. Elife *5*.

van den Pol, A.N. (2012). Neuropeptide transmission in brain circuits. Neuron *76*, 98-115.
Verma, S., Robertson, A.P., and Martin, R.J. (2007). The nematode neuropeptide, AF2 (KHEYLRF-NH2), increases voltage-activated calcium currents in Ascaris suum muscle. Br J Pharmacol *151*, 888-899.

Waggoner, L.E., Hardaker, L.A., Golik, S., and Schafer, W.R. (2000). Effect of a neuropeptide gene on behavioral states in Caenorhabditis elegans egg-laying. Genetics *154*, 1181-1192.

Wang, J., Chitturi, J., Ge, Q., Laskova, V., Wang, W., Li, X., Ding, M., Zhen, M., and Huang, X. (2015a). The C. elegans COE transcription factor UNC-3 activates lineage-specific apoptosis and affects neurite growth in the RID lineage. Development *142*, 1447-1457.

Wang, J., Kaletsky, R., Silva, M., Williams, A., Haas, L.A., Androwski, R.J., Landis, J.N., Patrick, C., Rashid, A., Santiago-Martinez, D.*, et al.* (2015b). Cell-Specific Transcriptional Profiling of Ciliated Sensory Neurons Reveals Regulators of Behavior and Extracellular Vesicle Biogenesis. Current biology : CB *25*, 3232-3238.

Weimer, R.M. (2006). Preservation of C. elegans tissue via high-pressure freezing and freeze-substitution for ultrastructural analysis and immunocytochemistry. Methods in molecular biology *351*, 203-221.

Wenick, A.S., and Hobert, O. (2004). Genomic cis-regulatory architecture and trans-acting regulators of a single interneuron-specific gene battery in C. elegans. Dev Cell *6*, 757-770.

White, J.G., Southgate, E., Thomson, J.N., and Brenner, S. (1986). The structure of the nervous system of the nematode Caenorhabditis elegans. Philosophical transactions of the Royal Society of London Series B, Biological sciences *314*, 1-340.

Xie, L., Gao, S., Alcaire, S.M., Aoyagi, K., Wang, Y., Griffin, J.K., Stagljar, I., Nagamatsu, S., and Zhen, M. (2013). NLF-1 delivers a sodium leak channel to regulate neuronal excitability and modulate rhythmic locomotion. Neuron *77*, 1069-1082.

Yanowitz, J.L., Shakir, M.A., Hedgecock, E., Hutter, H., Fire, A.Z., and Lundquist, E.A. (2004). UNC-39, the C. elegans homolog of the human myotonic dystrophy-associated homeodomain protein Six5, regulates cell motility and differentiation. Developmental biology *272*, 389-402.

Zahn, T.R., Macmorris, M.A., Dong, W., Day, R., and Hutton, J.C. (2001). IDA-1, a Caenorhabditis elegans homolog of the diabetic autoantigens IA-2 and phogrin, is expressed in peptidergic neurons in the worm. J Comp Neurol *429*, 127-143.

Zhen, M., and Samuel, A.D. (2015). C. elegans locomotion: small circuits, complex functions. Current opinion in neurobiology *33*, 117-126.

Table 1. Identification of Enriched Neuropeptide Transcripts in RID by Subtractive Transcriptome Profiling.

Sequence ID (Gene Name)	*wild-type* transcript counts (Mean±SD)		*unc-39* transcript counts (Mean±SD)		Enrichment in GFP cells (Fold)		P value (FDR-corrected)	
	All Cell Controls	GFP cells	All Cell Controls	GFP cells	*wild-type*	*unc-39*	*wild-type*	*unc-39*
Positive controls: similarly enriched in wild-type and *unc-39* GFP cells – transcripts known to be expressed by shared GFP cells								
Non-peptidergic								
W03A3.1 (*ceh-10)*	8.3 ± 5.8	121594.1 ± 561.1	7.0 ± 4.8	3132.3 ± 2037.8	191.1	445.1	9.74E-22	7.28E-08
C40H5.5a (*ttx-3)*	14.4 ± 6.8	1028.7 ± 402.9	17.3 ± 16.1	2323.0 ± 1331.1	71.4	134.6	3.21E-13	1.45E-07
ZC317.3 (*glc-3)*	63.9 ± 37.0	1139.2 ± 192.4	52.0 ± 40.9	2156.2 ± 1403.8	17.8	41.4	4.56E-16	3.57E-04
C02D4.2a (*ser-2)*	362.9 ± 83.6	4806.8 ± 1238.0	275.5 ± 92.6	7086.3 ± 3171.4	13.3	25.7	1.68E-14	1.38E-07
K03D10.1 (*kal-1)*	380.4 ± 118.1	1041.1 ± 40.2	411.3 ± 92.3	2136.0 ± 1192.0	2.7	5.2	0.02	0.02
Secreted								
C36B7.7 (*hen-1)*	16.1 ± 5.0	629.7 ± 239.4	22.6 ± 13.1	1218.2 ± 822.9	39.1	54.0	3.23E-11	4.22E-04
Related to neurotransmitters or neuromodulators								
W01C8.6 (*cat-1)*	87.3 ± 31.5	733.4 ± 121.4	60.1 ± 35.6	847.5 ± 272.7	8.4	14.1	1.48E-08	1.76E-09
ZC416.8 (*unc-17)*	200.0 ± 73.1	940.4± 104.2	265.0 ± 84.9	1254.3 ± 516.3	4.7	4.7	2.18E-05	1.26E-03
ZC416.8 (*cha-1)*	141.3 ± 31.1	422.1 ± 92.2	141.7 ± 80.3	565.7 ± 243.0	3.0	4.0	1.23E-02	4.72E-02
F48B9.4 (*pdf-2)*	89.4 ± 21.0	11535.6 ± 3721.3	76.5 ± 29.0	18096.1 ± 9039.8	129.0	236.7	3.33E-23	2.21E-11
T07E3.6a (*pdf-1)*	6652.6 ± 384.5	263951.0 ± 30655.9	8937.4 ± 1669.5	318710.4 ± 146449.1	39.7	35.7	4.67E-26	1.16E-07
T06C10.4 (*flp-10)*	6652.6 ± 384.5	263951.0 ± 30655.9	61.7 ± 38.2	2894.0 ± 1488.8	31.8	46.9	2.61E-21	1.24E-06
R09B5.13 (*cnc-11)*	11.7 ± 3.64	306.8 ± 190.9	20.1 ± 18.5	424.1 ± 216.3	26.3	21.1	5.15E-03	6.42E-05
CC4.2 (*nlp-15)*	1826.4 ± 237.8	27310.8 ± 2827.4	1886.8 ± 451.8	63296.2 ± 40301.7	15.0	33.6	4.04E-15	5.26E-04
C04H5.8a (*nlp-41)*	26.2 ± 14.9	378.4 ± 33.1	17.8 ± 2.6	587.9 ± 320.6	14.5	33.0	1.36E-11	2.52E-05
D1009.4a (*nlp-14)*	329.6 ± 64.3	4574.2 ± 788.3	362.0 ± 89.6	4781.8 ± 1977.6	13.9	13.2	7.35E-14	2.84E-06
C26F1.10 (*flp-21)*	28.0 ± 10.5	295.0 ± 37.0	65.4 ± 27.3	422.5 ± 172.9	10.5	6.5	4.15E-08	4.69E-04
VK10D6R.1 (*cnc-10)*	20.1 ± 3.4	171.3 ± 36.6	28.8 ± 13.4	604.3 ± 446.5	8.5	21.0	1.32E-05	0.01

F13B12.5 (*ins-1)*	70.1 ± 13.8	491.9 ± 93.3	37.9 ± 2.4	454.5 ± 180.8	7.0	12.0	1.29E-06	1.48E-06
Y48D7A.2 (*flp-18)*	37.8 ± 2.4	454.5 ± 180.8	282.4 ± 74.8	2604.1 ± 1174.6	6.2	9.2	5.84E-07	1.79E-04
Negative controls: not enriched in wild-type and *unc-39* GFP cells - transcripts expected to be absent from all GFP cells								
Muscle-specific								
T18D3.4 (*myo-2)*	3304.0 ± 1739.4	4457.8 ± 2753.5	3343.8 ± 1804.0	2801.5 ± 2571.1	1.4	0.8	1	1
K12F2.1 (*myo-3)*	3783.5 ± 1535.8	1423.6 ± 3783.5	1535.8 ± 1423.6	943.8 ± 3783.5	0.4	0.6	0.10	0.13
Other neurotransmitters								
ZK512.6a (*eat-4)*	209.3 ± 60.4	175.6 ± 74.5	160.8 ± 104.6	151.8 ± 61.9	0.8	0.9	1	1
Y37D8A.23a (*unc-25)*	6901.5 ± 2031.0	4499.3 ± 700.6	6901.5 ± 2031.0	4499.3 ± 701.0	0.6	0.6	1	0.74
Candidates for RID-enriched transcripts: preferentially enriched in wild-type GFP cells								
Non-peptidergic (positive controls – transcripts known to be present in RID)								
Y48A6A.1 (*zig-5)*	282.4 ± 74.8	2604.1 ± 1174.6	93.6 ± 32.1	560.0 ± 545.1	15.8	6.0	4.85E-14	0.35
ZC64.4 (*lim-4)*	137.3 ± 13.9	1558.5 ± 637.5	95.3 ± 29.5	783.9 ± 697.6	11.4	8.2	1.01E-05	0.17
Peptidergic (RID enriched)								
F56F3.6 (*ins-17)*	34.4 ± 10.5	265.6 ± 37.8	56.0 ± 17.8	101.7 ± 68.7	7.7	1.8	2.37E-06	0.72
Y37D8A.15 (*flp-14)*	2917.5 ± 368.0	19547.2 ± 586.8	3427.3 ± 1069.2	8562.1 ± 6291.9	6.7	2.5	7.55E-08	0.53
B0213.17 (*nlp-34)*	9.8 ± 6.5	67.0 ± 23.2	13.3 ± 6.5	37.8 ± 35.3	6.8	2.8	0.01	0.67

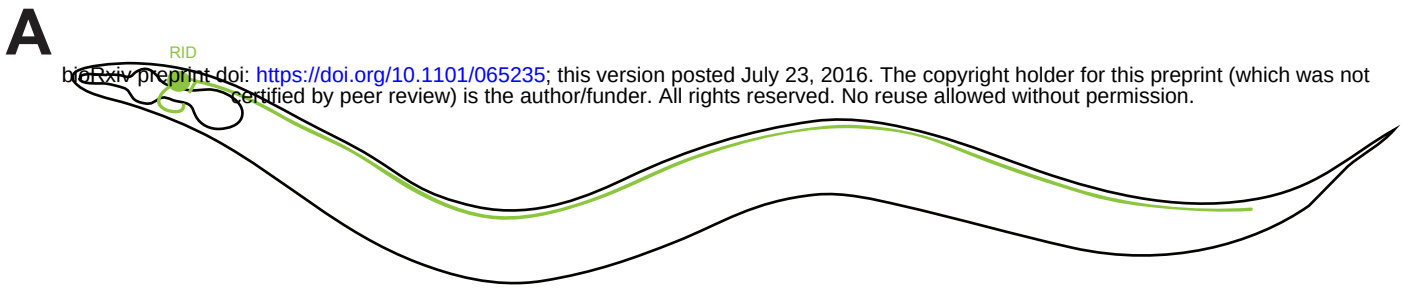

Figure 1

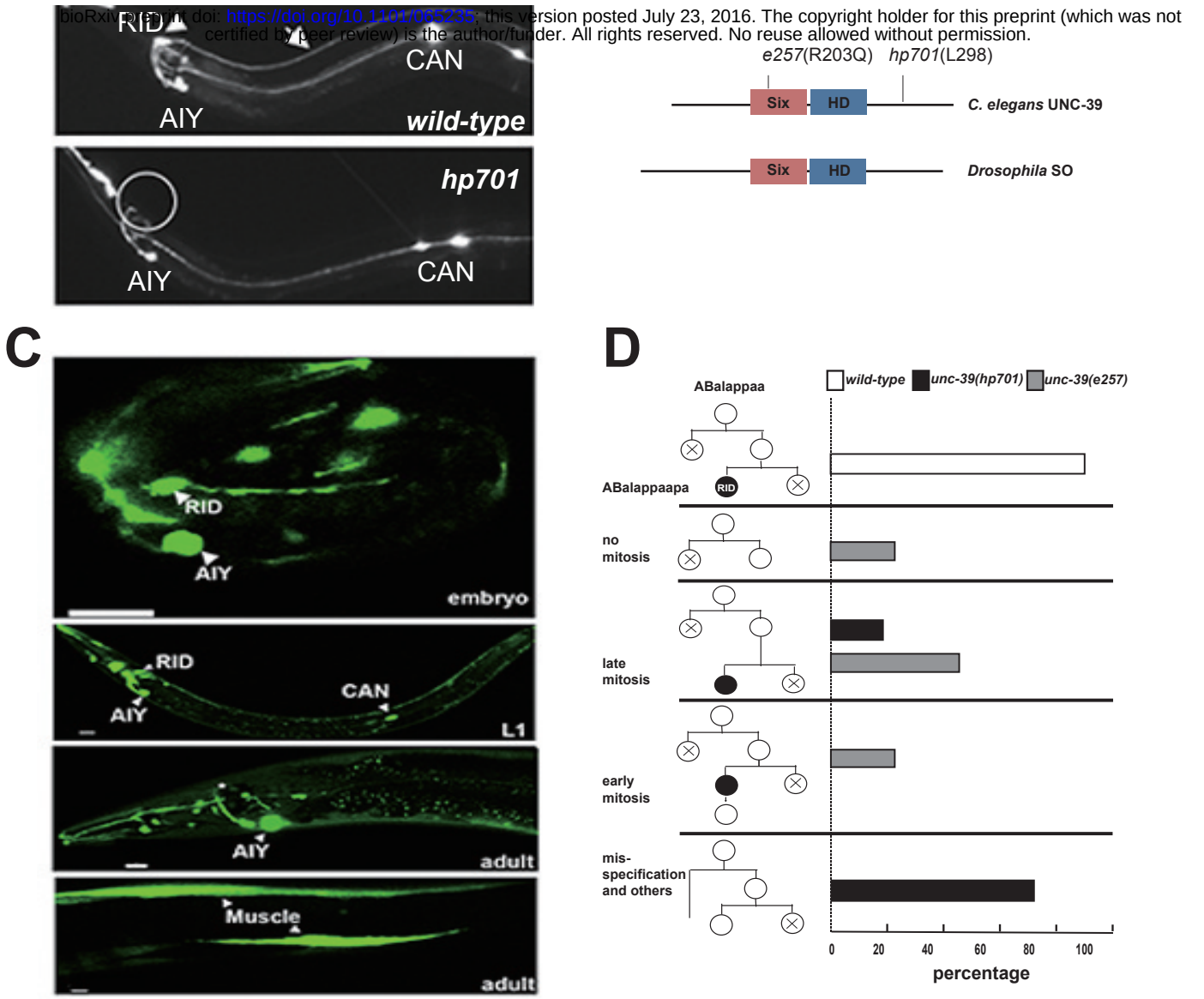

Figure 2

A

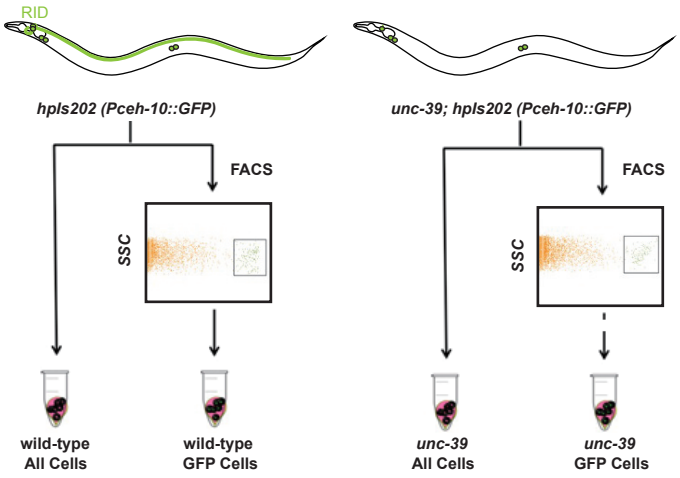

B

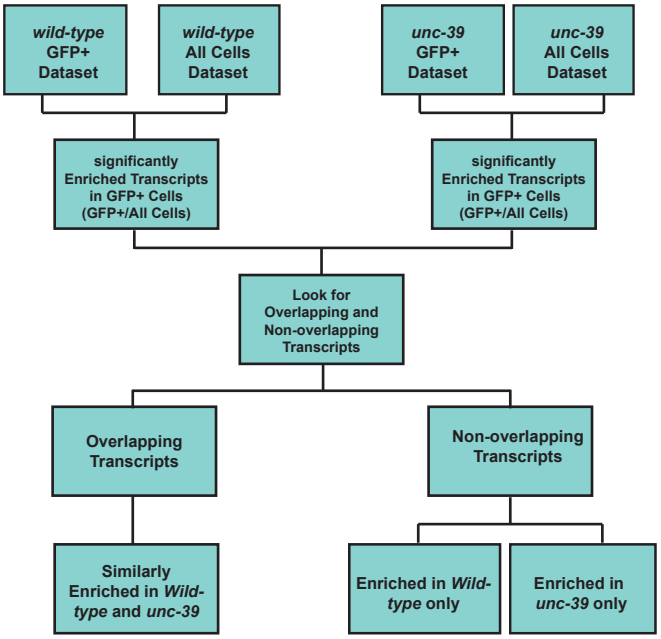

C

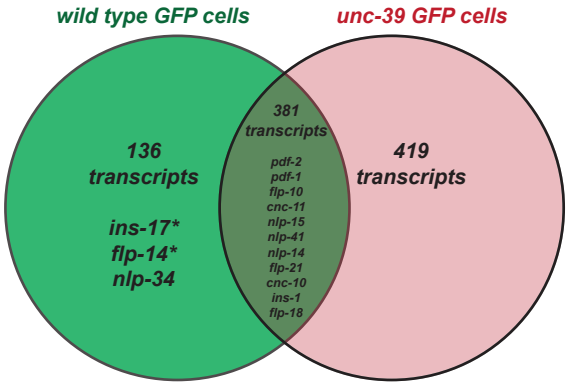

D

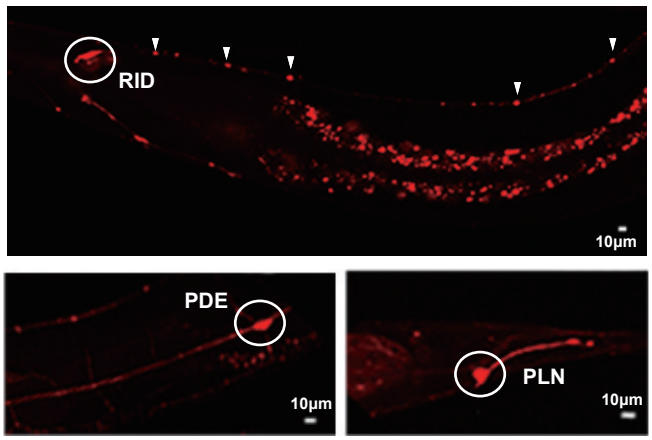

E

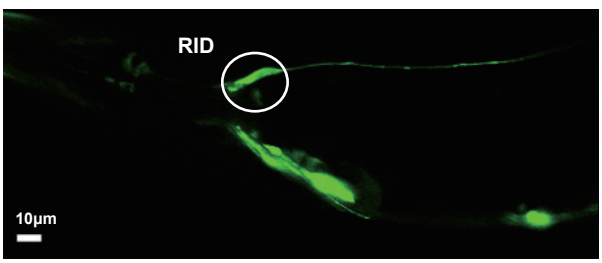

Figure 3

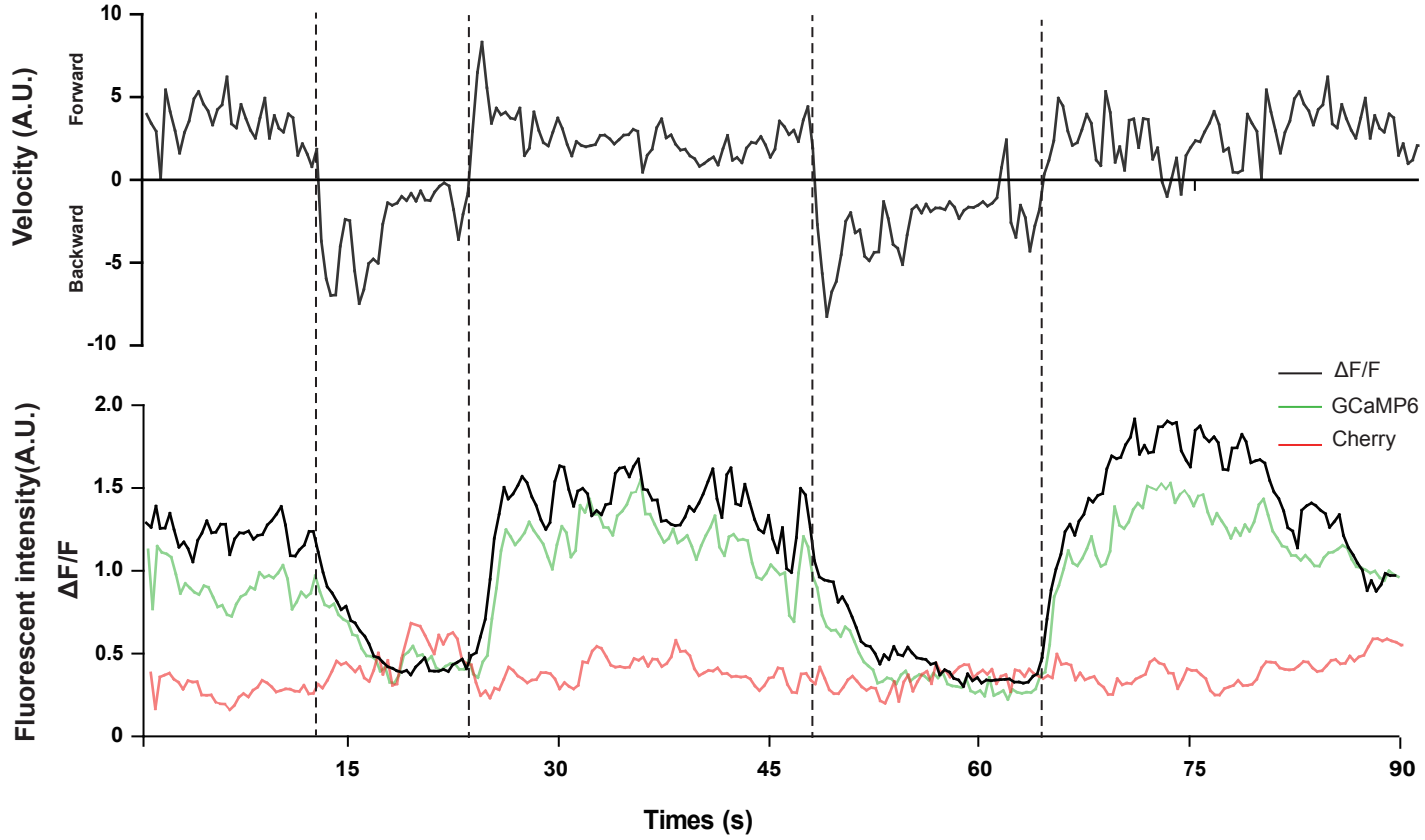

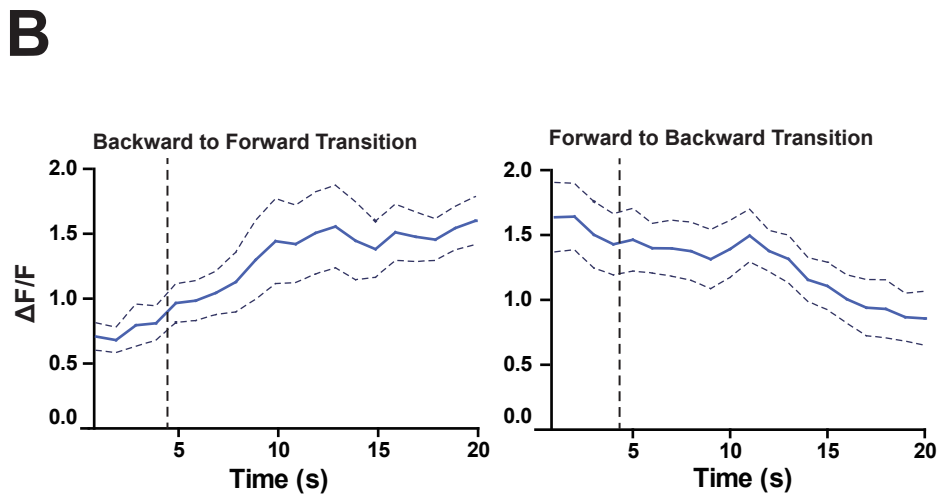

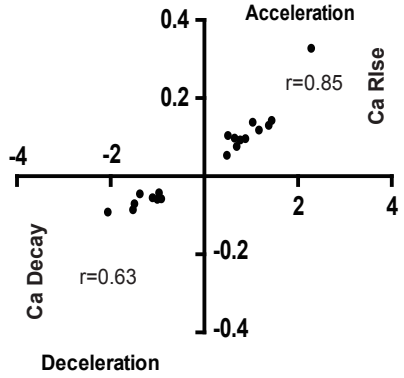

Figure 4

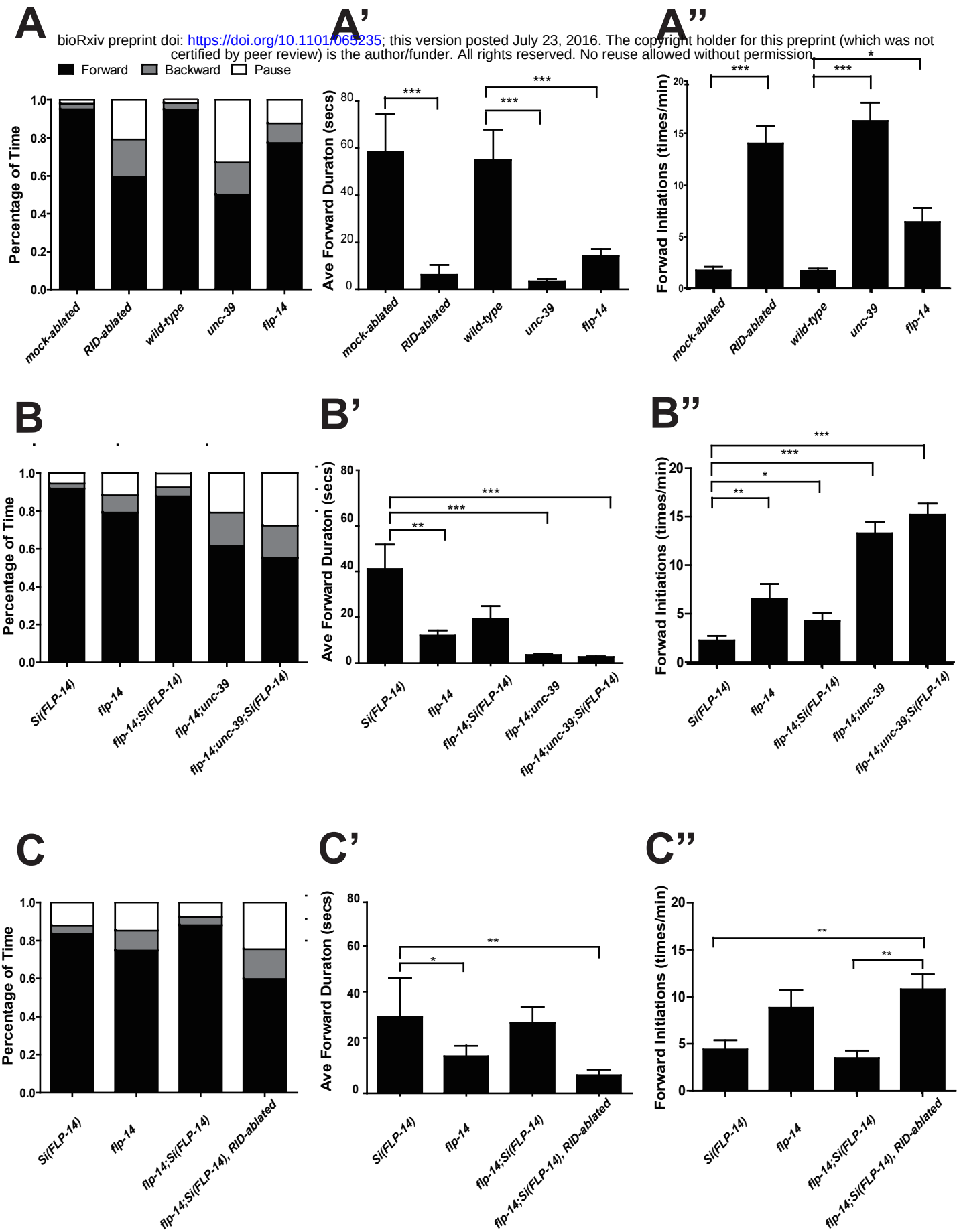

Figure 5

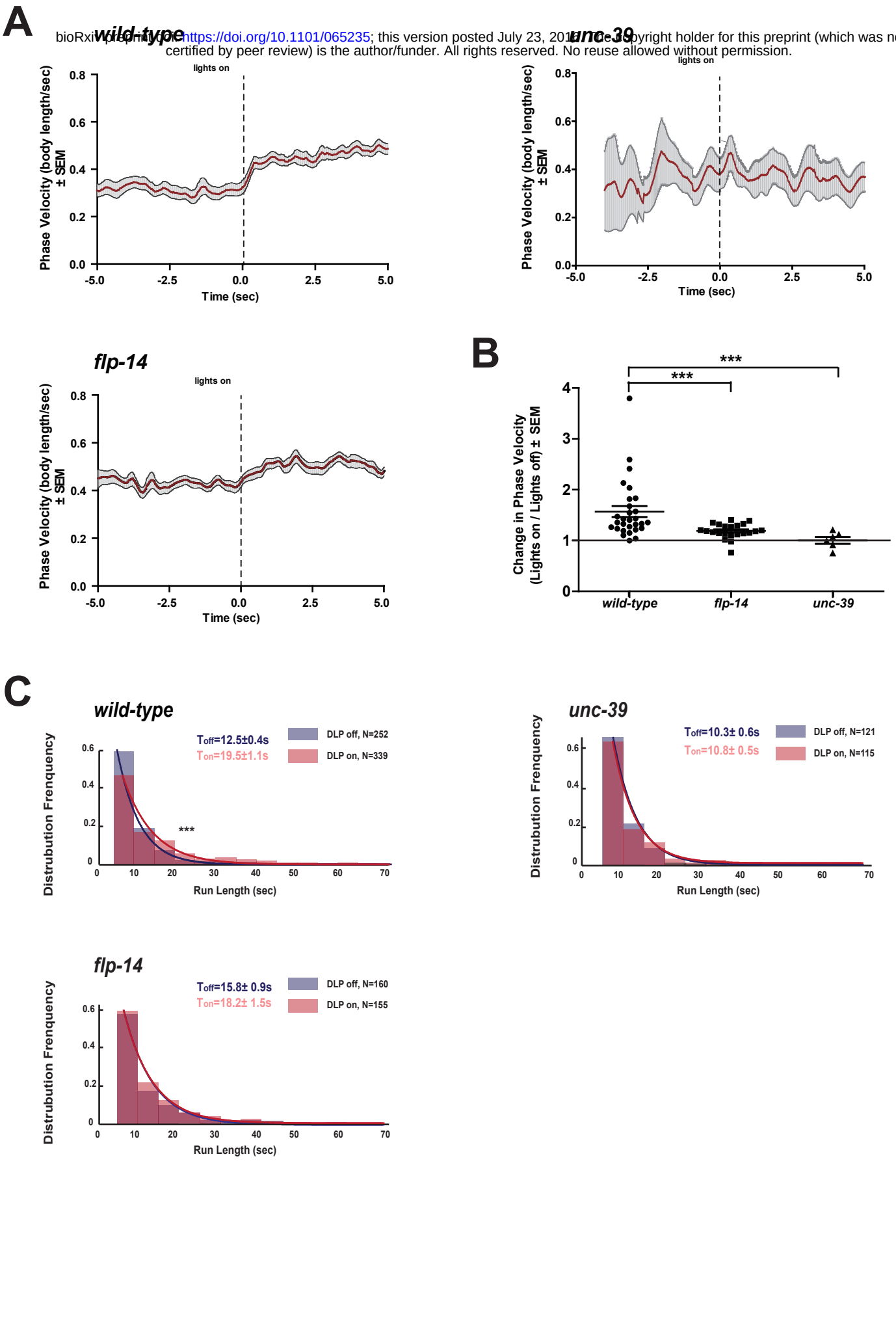

Figure 6

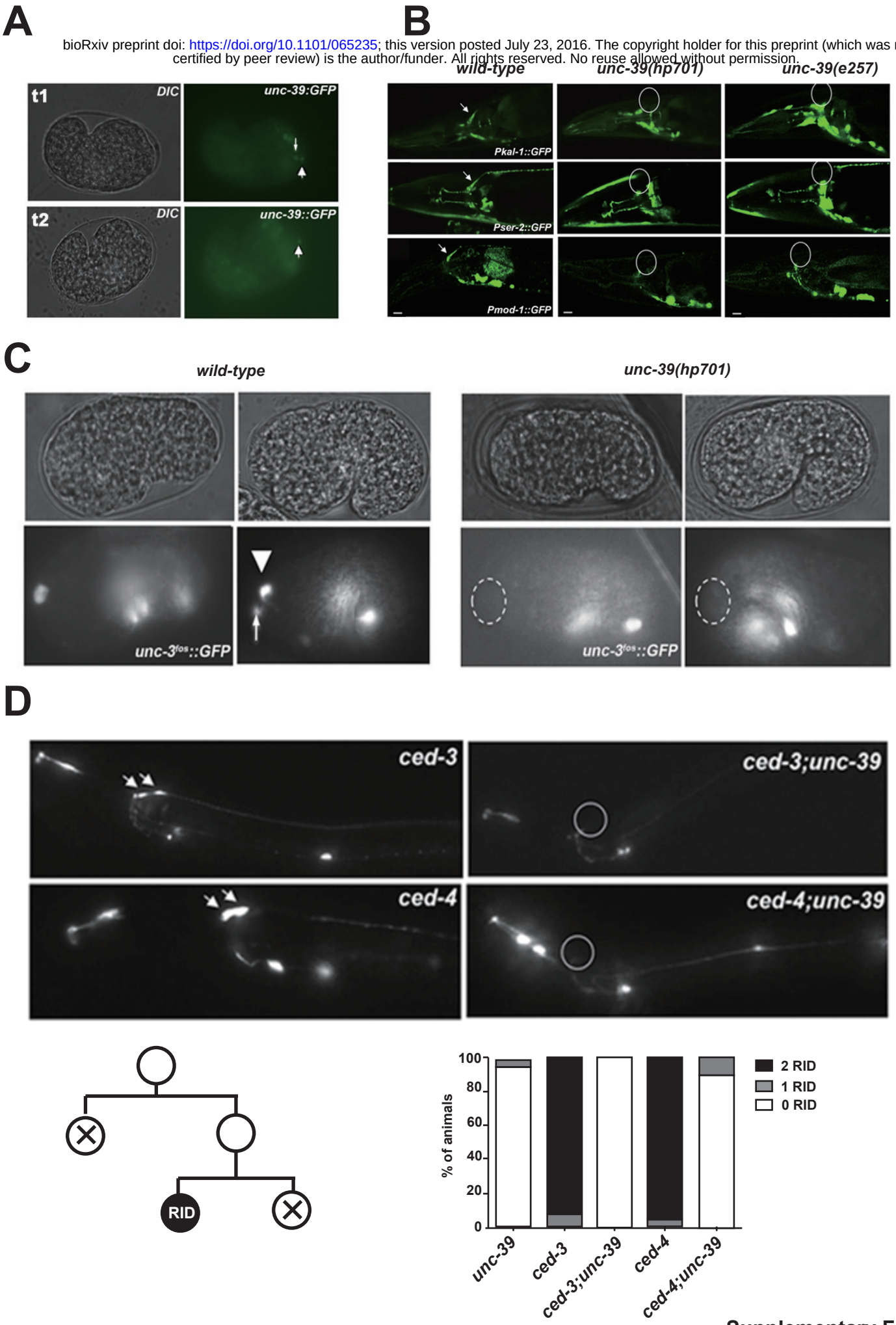

Supplementary Figure 1

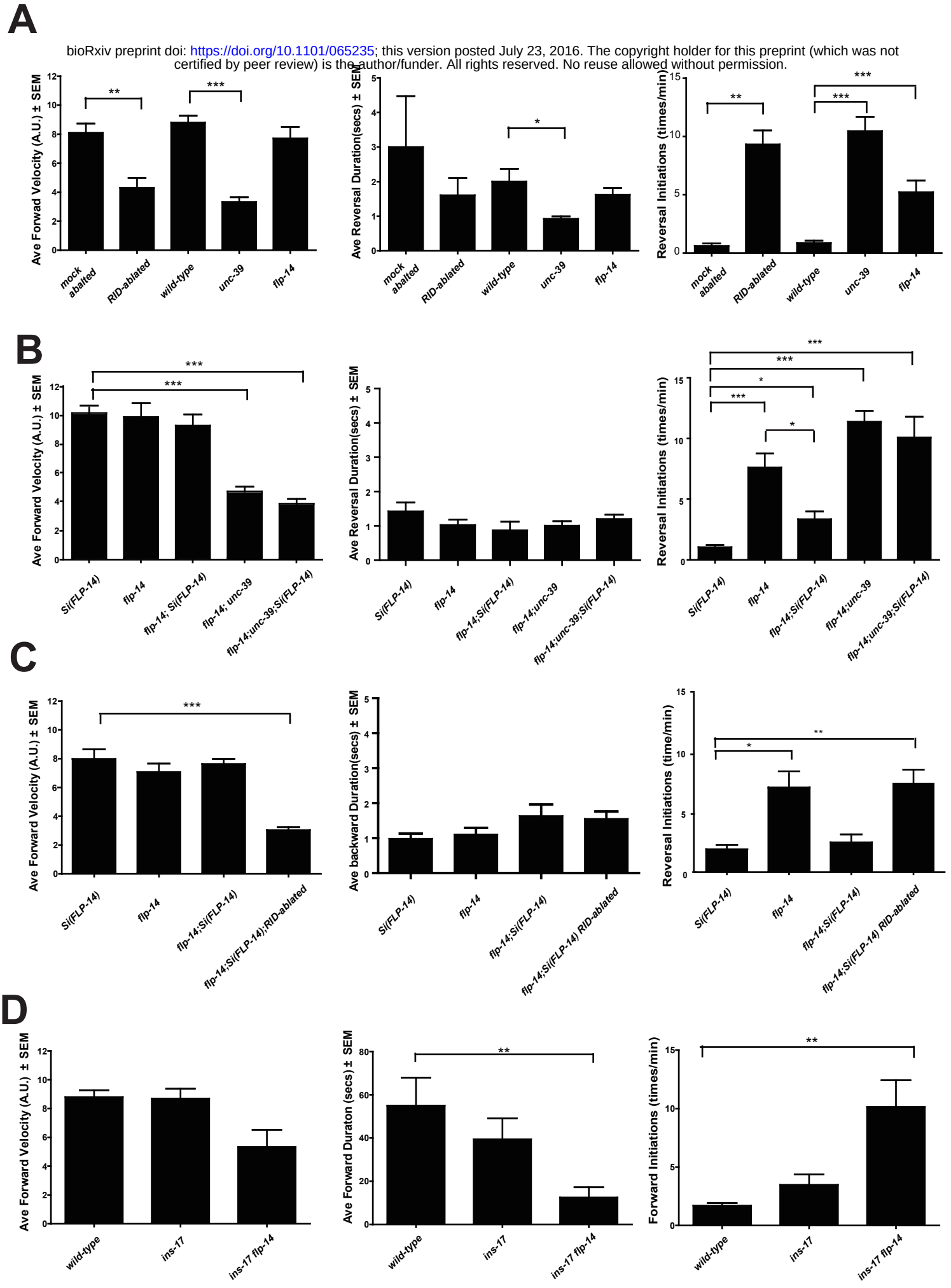

Supplementary Figure 2

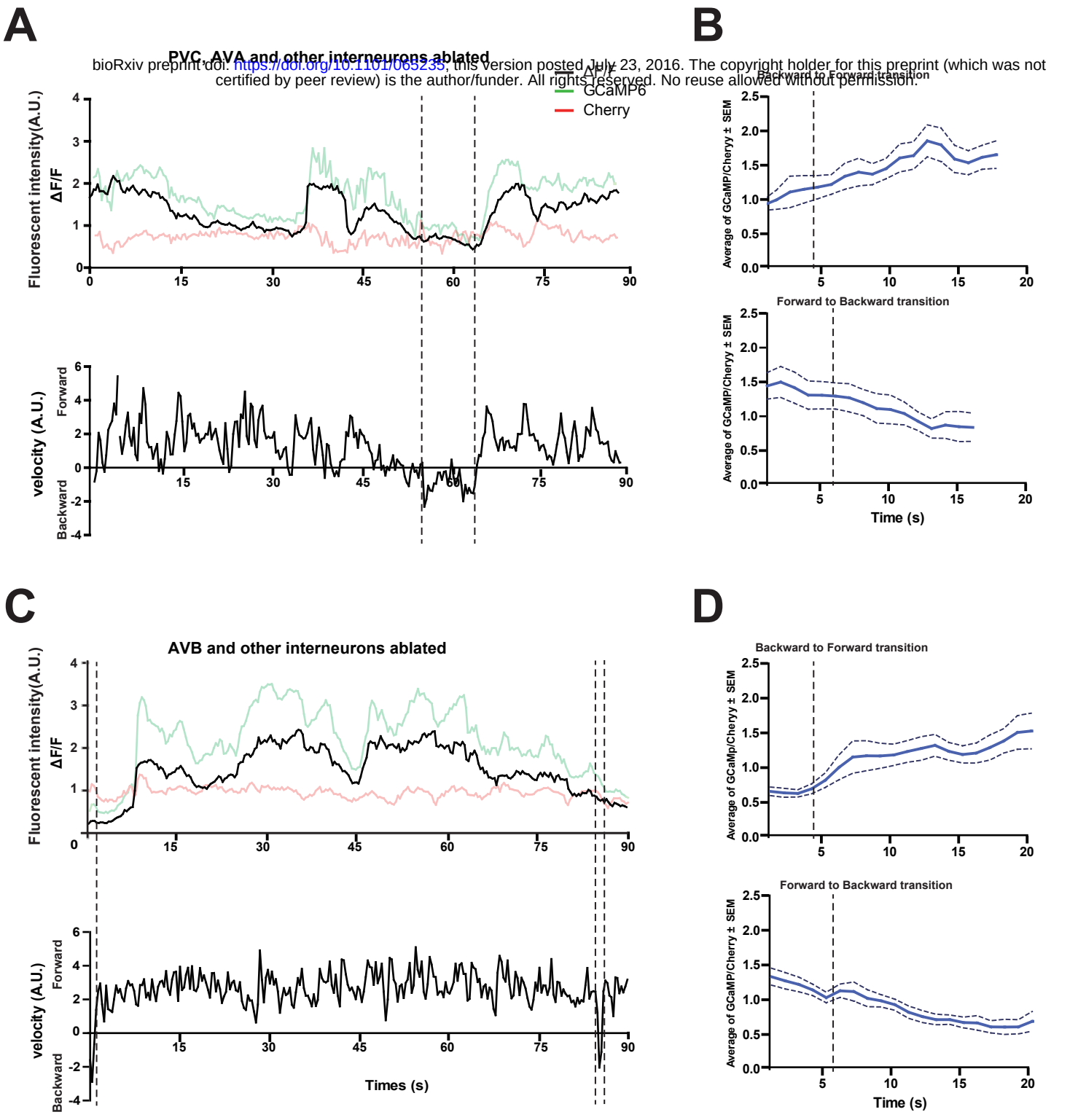

Supplementary Figure 3

A

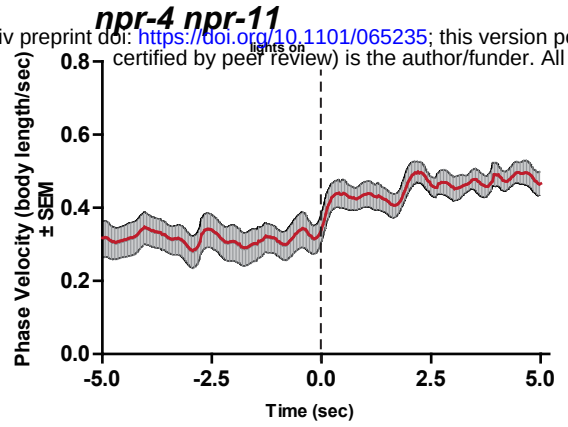

B

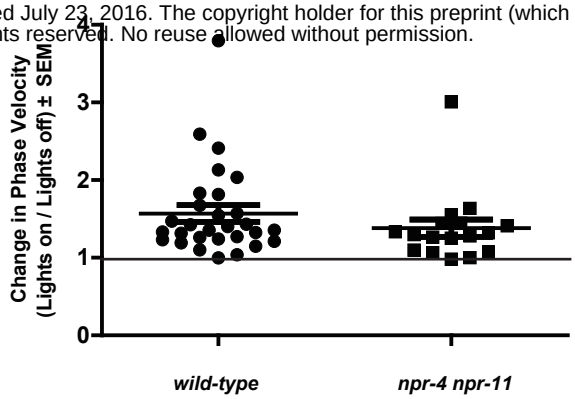

C

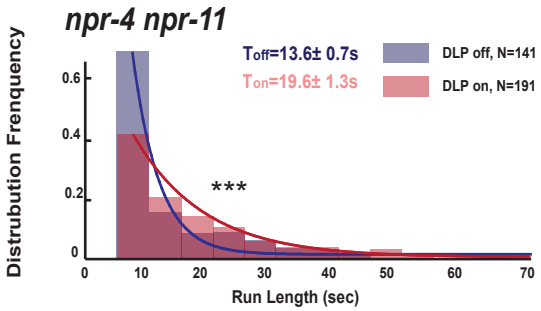

Supplementary Figure 4

Supplemental Information

Supplemental Figure Legends

Figure S1. The expression pattern of UNC-39::GFP and phenotypes of *unc-39* mutants.

A. During embryogenesis, *unc-39::GFP* is expressed in both RID (arrowhead) and the RID sister cell (arrow) (t1), before the latter dies as a result of apoptosis (t2).

B. Known RID cell fate markers, such as *kal-1* (B^1), *ser-2* (B^2), and *mod-1* (B^3) are present in wild type animals (arrow), but not *unc-39* mutants *hp701* and *e257*.

C. During early embryogenesis, the RID lineage-specific apoptosis activator UNC-3 is expressed in RID and the RID sister cell, but not in *unc-39* mutants.

D. The absence of RID in *unc-39* mutants is not due to ectopic apoptosis. **D^1**. A schematic of the RID cell lineage: the ABalappaa neuroblast undergoes two consecutive rounds of mitosis to give rise to RID. Both the sisters of the RID precursor and RID undergo apoptosis**. D^2.** Apoptotic mutants *ced-3* and *ced-4* possess two RID neurons resulting from failure to activate apoptosis in the RID sister (arrowheads). However, a majority of *unc-39; ced-3* and *unc-39; ced-4* mutants still do not possess RID. For **B**, **C**, and **D**, the putative position of RID and/or RID sister cell in *unc-39* mutants is designated by a circle. **D^3.** Quantification of genetic interaction in **D^2**, N=10 animals per genotype.

Figure S2. Spontaneous motor behaviors of animals of respective genotypes.

A. A comparison of the mean forward velocity, reversal duration and reversal re-initiation frequency between the wild-type (*Pceh-10* marker strain), mock-ablated and RID ablated, wild-type (N2), *unc-39(e701)* and *flp-14* animals. N=10 animals/per genotype, and data presented in each group (in A-D) were collected on the same day, on the same plate. RID-ablated animals and *unc-39* exhibit decreased forward velocity and increased re-initiation of reversals.

B. A comparison of wild-type (*Si(FLP-14)*), *flp-14, flp-14;Si(FLP-14), unc-39;flp-14, unc-39;flp-14;Si(FLP-14)* animals shows deceased forward velocity and increased re-initiation of reversals in the *unc-39* background.

C. A comparison of the motor phenotypes of RID ablation in *flp-14; Si(FLP-14)* background show significantly reduced forward velocity and increased reversal initiations.

D. *ins-17* animals did not exhibit significant motor behavioral changes.

Figure S3. The loss of PVC or AVB alone does not abolish RID activity rise during forward movement.

A. A representative velocity trace (top) and corresponding RID calcium activity trace (bottom) from a moving animal with PVC (and other neurons) ablated. Raw fluorescence intensities of GCaMP and cherry, as well as normalized ratiometric (GCaMP/cherry) change (ΔF/F), are shown. (ΔF/F) is used to an index for the calcium activity change. Changes in positions of fluorescent signals are used to calculate velocity and directionality. Dotted longitudinal lines indicate transition period between backward to forward locomotion.

B. RID activity as measured by ΔF/F ± SEM during transition periods in PCV (and other neurons)-ablated animals. RID activity increases when animals transition from backward to fast forward locomotion, and decreases when animals transition from forward to backward locomotion. Dotted longitudinal lines indicate transition period between backward to forward locomotion.

C, D. The same analyses as in A-B, except that experiments were performed in animals where AVB (and other neurons) were ablated.

E, F. Cross-correlation between the change in RID activity, and the change in velocity in PVC (and other neurons) (**E**) and AVB (and other neurons) ablated animals (**F**). Positive and negative slopes (Y-axis) indicate increase and decrease in RID activity, respectively. Positive and negative values on the X-axis indicate changes in velocity from backward to forward locomotion (acceleration) and from forward to backward locomotion (deceleration), respectively. For **B, D, E** and **F,** N=9-10 transitional events.

Movie S1. Thirty-two consecutive serial sections of a part of the dorsal nerve cord in adult wild-type animals. The RID process in the dorsal nerve cord is outlined in pink, and the DD axon is outlined in green.

Movie S2. Changes in the RID calcium transients in moving animals. RID activity increases during period of acceleration during forward bout, or during transitions from reversal to fast forward locomotion. Left panel: RFP; Right panel: GCaMP6. Note that multiple neurons expressed GCaMP6::RFP, but only RID (soma and axon) exhibited signal increase that was correlated with increased forward locomotion.

Movie S3. Representative video of a L4 stage wild-type (N2) animal on an NGM plate with a thin-layer of OP50 bacteria food.

Movie S4. Representative video of a L4 stage *unc-39(hp701)* animal on an NGM plate with a thin-layer of OP50 bacteria food.

Movie S5. Representative video of a L4 stage *flp-14(gk1055)* animal on an NGM plate with a thin-layer of OP50 bacteria food.

Movie S6. Representative video of a young adult ZM9315 (RID-specific Chrimson) animal on a thin NGM plate without food, upon RID optogenetic stimulation while the animal was doing forward movement.

Movie S7. Representative video of a young adult ZM9315 (RID-specific Chrimson) animal on a thin NGM plate without food, upon RID optogenetic stimulation during reversals.

Supplemental Methods

A List of Genetic Mutant Strains Generated and Used

Gene	Allele	Strain
unc-39 V	*hp701*	ZM6539

unc-39 V	*e257*	CB257
ced-3 IV	*n717*	ZM6097
ced-4 III	*n1162*	ZM6098
unc-3 X	*xd86*	ZM9343
flp-14 III	*gk1055*	ZM8969
ins-17 III	*tm790*	ZM2860
Ins-17 flp-14 III	*tm790 gk1055*	ZM9030
snf-11 V	*ok156*	RM2710
flp-14III; snf-11V	*gk1055; ok156*	ZM9215
npr-4 X	*tm1782*	ZM9455
npr-11 X	*ok594*	ZM9454
npr-4 npr-11 X	*tm1782 ok594*	ZM9455

A List of Constructs and Transgenic Strains Generated and Used

(LIN-15 was used as an injection marker if not specified)

Experiment	Plasmid	Description (injection marker)	Background	Transgene	Strain
RID Reporters	pJH2103	*Pceh-10::GFP*	*lin-15(n765)*	*hpIs202* *hpIs201*	ZM5488 ZM5489
	pJH1647	*Pceh-10::Cherry*	*lin-15(n765)*	*hpIs292*	ZM6905
	pJH1647	*Pceh-10::Cherry (pRF4)*	*juIs1*	*hpIs162*	ZM8000
	pJH2160 pJH2247	*Pceh-10::IDA-1::Cherry* *Pceh-10::ins-22::GFP*	*lin-15(n765)*	*hpEx3669*	ZM8823
	pJH2247 pJH2160	*Pceh-10::ins-22::GFP* *Pceh-10::IDA-1::Cherry*	*lin-15(n765)*	*hpEx3669*	ZM8823
	Hobert lab	*Pkal-1::GFP*	*unknown*	*otIs33*	OH904

	Hobert lab	*Pser-2::GFP*	*unknown*	*otIs107*	OH2246
	pJH2715	*Pmod-1::mito::GFP*	*lin-15(n765)*	*hpIs274*	ZM6658
	Huang lab	*unc-3 fosmid::SL2::GFP (sur-5::RFP)*	*unc-3(xd86); hpIs162*	*xdEx1091*	XD2319
unc-39 Related	pJH2765	*Plim-4::lim-4::GFP*	*lin-15(n765)*	*hpEx3035*	ZM7100
	pJH2839	*Punc-39::GFP*	*lin-15(n765)*	*hpIs328*	ZM7150
	pJH2798	*Genomic unc-39 minimal rescuing clone*	*unc-39(hp701); hpIs292*	*not maintained*	*not maintained*
	pJH3138	*unc-39fosmid::GFP (Pmyo-3::RFP)*	*unc-39(e257)*	*hpEx3186*	ZM7572
	pJH2811	*Punc-39::UNC-39::GFP (RF4)*	*unc-39(hp701); hpIs292*	*hpEx3034*	ZM7482
	pJH2839	*Punc-39::GFP*	*lin-15(n765)*	*hpIs328*	ZM7150
	pJH3366	*Punc-39::unc-3 cDNA (RF4)*	*unc-39(hp701); hpIs202*	*hpEx3498*	ZM8312
	pJH3084 pJH3366	*Punc-39::LIM-4 cDNA::GFP Punc-39::UNC-3 cDNA*	*unc-39(hp701); hpIs292*	*not maintained*	*not maintained*
flp-14 Related	pJH3884	*flp-14 genomic miniMos (Neo^R)*	*wt*	*hpSi38*	ZM9518
			flp-14(gk1055)	*hpSi38*	ZM9474
			flp-14(gk1055); unc-39(hp701)	*hpSi38*	ZM9468
			hpIs201	*hpSi38*	ZM9473
			flp-14(gk1055); hpIs201	*hpSi38*	ZM9519
	pJH2103	*Pceh-10::GFP*	*flp-14(gk1055)*	*hpIs201*	ZM9502
flp-14 ins-17 reporters	pJH3608	*Pflp-14::GFP*	*lin-15(n765)*	*hpEx3695*	ZM8935
	Hutter lab	*Pins-17::GFP (unc-119)*	*unc-119(ed3)*	*wwEx73*	HT1734
	pJH3644	*Pflp-14::GCaMP6::Cherry*	*lin-15(n765)*	*hpIs587*	ZM9078
			hpIs321	*hpIs587*	ZM9312

Calcium Imaging			*juIs440*	*hpIs587*	ZM9404
Optogenetic Stimulation	pJH3790 pJH3796 pJH3774	*Pceh-10::Chrimson::GFP::ZF* *Pttx-3::ZIF-1::SL2::RFP* *Pgpa-14::ZIF-1::SL2::RFP*	*lin-15(n765)*	*hpIs626*	ZM9331
	pJH3835	*Parr-1-ZIF-1::SL2::RFP*	*hpIs626*	*hpEx3808*	ZM9351
			unc-39(hp701); hpIs626	*hpEx3808*	ZM9472
			flp-14(gk1055); hpIs626	*hpEx3808*	ZM9476

Electron Microscopy Analysis

Images were stitched and aligned using TrakEM2 (Cardona et al., 2012). In the L1 animal, all neurons were identified based on cell body position (Sulston et al., 1983), synapse pattern and neurite trajectory (White et al., 1986). In the adult EM reconstruction, all neurons were identified by characteristic synapse patterns and trajectories (White et al., 1986). Volumetric reconstruction of neurons was performed using TrakEM2 and skeleton tracing using CATMAID (Saalfeld et al., 2009) followed by rendering in Blender (http://www.blender.org).

Fluorescence Microscopy and Confocal Imaging

For imaging dense core vesicle (*Pceh-10-IDA-1::cherry)* and neuropeptide fluorescent markers (*Pceh-10-INS-22::GFP)*, expression patterns of UNC-39 (*Punc-39-GFP, Punc-39-UNC-39::GFP)* and RID phenotypes in *unc-39* mutants using RID fluorescent markers *(Pceh-10::GFP)* and RID cell fate markers (*Pkal-1-GFP, Pser-2-GFP, Pmod-1-GFP)*, images were captured using a 63x objective on a Zeiss Axioplan 2 connected to a Hamamatsu ORCA-ER digital camera and processed using Improvision Open Lab software. Images were processed using minimal deconvolution levels to remove background fluorescence. Confocal images of transgenic strains carrying either *Pflp-14-GFP*, *Pins17-GFP*, *unc-3fosmid::SL2::GFP*, and *unc-39fosmid::GFP* were

acquired on a Nikon Eclipse 90i confocal microscope. Confocal image processing was conducted using Adobe Photoshop.

Larval Cell Extraction and Cell Sorting

Briefly, synchronized animals were pelleted and thoroughly washed with M9 Buffer to remove bacterial contamination. Prior to extraction, an aliquot of sample was flash-frozen in liquid nitrogen to be used as the All Cells reference sample for subsequent transcriptome analysis. To the remaining sample, freshly thawed SDS-DTT solution (0.25% SDS, 200 mM DTT, 20 mM HEPES, 3% sucrose pH=7.5-8.0), which softens the cuticle, was added for no longer than 4 minutes (or until majority of animals started twitching, but did not become completely rod-like or rigid). Post-incubation with SDS-DTT, the sample was neutralized and washed 5x times with 1x Egg Buffer. To break apart animals, Pronase solution (15 mg/mL) was added, and the sample was pipetted ~40x for 30 minutes. After several washes, cells were resuspended in 1x Egg buffer. Propidium iodide (1ug/mL) was added prior to cell sorting to identify damaged cells.

GFP+ cells from L2 worms were sorted onto Trizol-LS (Invitrogen) using a BD FACSAria with a 70 micron nozzle (BD Biosciences) operated at the University of Toronto Flow Cytometry Facility. Profiles of GFP+ strains were compared to an N2 standard to identify and exclude autofluorescent cells. For each independent replicate, 20,000-50,000 events, most likely representing cells, were FACS-isolated from each strain. Three and four biological replicates with corresponding All Cells reference samples were collected for the *hpIs202* control and *the unc-39 (hp701); hpIs202* strains, respectively.

RNA-sequencing Preparation and Analysis

RNA Extraction

For the all cells reference samples, flash-frozen pellets were pulverized using a mortar and pestle and dissolved in Trizol-LS (Invitrogen). RNA was extracted from these pulverized worm pellets (All and from sorted cells collected directly in Trizol-LS (GFP+ cells sample). DNA

contamination was removed using the Zymo DNA-free RNA Kit (Zymo Research) according to manufacturer's instructions.

Library Preparation and RNA-sequencing

RNA sample concentration and quality were determined using an Agilent Bioanalyzer at The Centre for Applied Genomics (SickKids Hospital, Toronto, ON, Canada). RNA Integrity Numbers (RIN) scores of 7 and above were used for subsequent RNA-sequencing analysis. RNA concentration was also verified using the Quibit RNA HS Kit (Thermo Fisher Scientific).

5 ng of RNA was used as starting material for cDNA library preparation. cDNA was synthesized from RNA using the SMARTer Ultra Low Input RNA Kit for Sequencing (Clontech) and cDNA libraries prepared using the Low Input DNA Library Prep Kit (Clontech) according to manufacturer's instructions. RNA-sequencing was performed on an Illumina Hiseq 2000 according to standard protocols, generating 100 base paired-end reads.

Bioinformatics Analysis

Sequencing reads were mapped to the *C. elegans genome* (WS235) using RNA STAR under default settings (Dobin et al., 2013). Using these conditions on RNA STAR, 75-80% of reads aligned to a unique transcript. Gene expression quantification and differential expression were analyzed using HTSeq (Anders et al., 2015) and DESeq (Anders and Huber, 2010), respectively, under default settings.

Using DESeq, we identified differentially expressed transcripts between GFP+ cells and All Cells reference samples in the *hpIs202* and *unc-39(hp701);hpIs202* datasets. For *hpIs202* and *unc-39(hp701);hpIs202* datasets, transcripts were considered significantly enriched in GFP+ cells over sample matched All Cells by applying the following criteria or filters: 1) Differentially expressed transcripts with False Discovery Rate (FDR) adjusted p values < 0.05, and, 2) Transcripts where the ratio of log2 transformed Mean Counts from GFP+ samples to log2 transformed Mean Counts from All Cells samples was greater than 1 (Mean GFP+ Counts / Mean

All Cells Counts > 1). Final datasets resulted from analyses of >3 experimental replica from All cells and GFP+ samples for wild-type and *unc-39* mutant strains.

Locomotion Behavior Analysis

Behavior Acquisition and Tracking

When transferred to a new, thinly seeded plate, *C. elegans* typically spend most of the time moving forward, with brief interruptions of backward movement. As previously described with some modifications (Gao et al., 2015), 35 mm NGM plates with limited food (lightly seeded OP50 bacteria) were used for automated tracking and behavioral analyses. Using this method, we quantified the percentage of time animals spent moving forward, backward, and pausing. We also quantified initiation frequency, duration, and velocity of larval stage 4 (L4) animals. For RID-ablated animals, controls were mock-ablated animals carrying the same reporter. For *unc-39, flp-14*, *ins-17*, and *snf-11* genetic mutants, controls were N2 animals.

Prior to recording, animals were placed in the center of a 50 mm lightly seeded NGM plate and allowed to habituate for 5 minutes prior to recording. Behavior was recorded for 3 minutes under a 40x objective using a 20Zeiss Axioskop 2 Plus equipped with an ASI MS-40000 motorized stage and a CCD camera (Hamamatsu Orca-R2).

Tracking and analysis were performed using Micromanager and ImageJ software plugins developed in-house (courtesy of Dr. Taizo Kawano). Image sequences were sampled at 100-msec exposure (10 frames per second). The directionality of movement (forward vs. backward) was determined by first identifying the anterior-posterior axis or the “head” and “tail” points, which were manually defined at the first two frames and verified throughout the recording. To calculate directionality of movement, the displacement of the midline point in relation to the head and tail for each worm was determined based on its position in the field-of-view and the stage coordinates. Image sequences where animals touched the edge of the recording field or crossed over on themselves were not processed.

Quantification and Data Analyses

Analyses of the output data were carried out using an R-based code developed in-house (courtesy of Dr. Michelle Po). The following parameters were quantified by the program: 1) Initiation (defined as the frequency of directional change for each animal); 2) Duration (defined as the time spent moving in the same direction for >3 frames or 300msec, calculated for each bout of forward or backward initiation); 3) Velocity (defined by the speed, displacement of animal divided by the # of frames, and directionality of the animal). Frequency of initiations, durations, and velocities were calculated for forward and backward locomotion separately.

Calcium Imaging and Data Analysis

Regions of interest (ROIs) containing the RID neuron was defined using a MATLAB script developed in-house. GCaMP and RFP fluorescence intensities from RID were then measured. To analyze overall RID activity, the ratio of GCaMP to RFP was calculated in order to control for possible motion artifacts detected. The velocity of each time point was measured using an Image J plug-in developed in-house (Gao et al., 2015; Kawano et al., 2011). The rate for Acceleration during each transition from backward to forward locomotion was calculated by subtracting the lowest velocity point during backward locomotion from the highest velocity point during forward locomotion, and normalizing it to the number of frames in-between these two points ($Velocity_{peak}$ – $Velocity_{trough}$ / # of Frames). The rate of Deceleration during transitions from forward to backward locomotion was calculated similarly ($Velocity_{trough}$ – $Velocity_{peak}$ / # of Frames). Rise and decay in calcium transients during transitions from backward to forward locomotion and vice versa, respectively, were calculated using the linear slope. Cross-correlation analyses were performed between rate of acceleration and calcium rise, as well as deceleration and calcium decay.

Optogenetic stimulation and data analyses

To make OP50-retinal plates, we seeded each 60 mm NGM plate with a mixture of 250 μl OP50 in LB with 1 μl of 100mM retinal in ethanol. L4 stage animals that carried two transgenes, which exhibited restricted expression of Chrimson at RID (*hpIs626; hpEx3808*) were cultivated on OP50-retinal plates at 20°C in darkness for ~24 hours. Animals were then individually washed in

the NGM buffer before allowed to navigate on the surface of a 100 mm NGM plate without food. We used the Colbert system to stimulate Chrimson with a Diode red laser (MRL-III-635, 635 nm wavelength, 200mW maximum power, CNI Laser) and carry out dark-field imaging using infrared light and a dark field condenser (Nikon) using a 10X Plano Apo objective (NA=0.45). A motorized stage and custom real-time computer vision software kept the animal in the center of the field of view. The locomotion of each animal was recorded for 30 min or until it reached the edge of the plate. The laser was set at a 3 min on / 3 min off cycle during the recording. Data was collected at 30 f/s and analyzed using a customized particle-tracking and shape analysis algorithms. Each trajectory was segmented into periods of forward movement (runs) separated by sharp orientations (turns). Turns were automatically flagged when the heading change of the center of the mass trajectory was $>60^{o}$ over 1 sec. To quantify the change of phase velocities before and after the laser was switched on (Figure 6A, B), we selected events when the laser was on during a run with at least 5 sec of forward movement before and after the switch. To quantify the run length, all runs during the laser on phase and laser off phase were included.

Statistical Analysis

For locomotion (# of initiations, durations, velocities), statistical significance was determined using Mann-Whitney or Kruskal-Wallis tests for comparing two and more than two variables, respectively, and subjected to post-hoc analysis. For calcium imaging (correlations between acceleration/deceleration and rise/decay of calcium transients), Pearson tests were used to calculate correlation coefficients and statistical significance. For optogenetic stimulation and locomotion analyses, Wilcoxon matched-pairs signed rank test was used to compare the velocity difference during periods of Lights On and Off of the same strain. The Kruskal-Wallis Test with post-hoc test (Dunn's Multiple Comparison) was used to assess the significance of difference between groups. $P< 0.05$ were considered to be statically significant. All statistics were performed using Prism software (GraphPad).

Supplemental References

Anders, S., and Huber, W. (2010). Differential expression analysis for sequence count data. Genome biology *11*, R106.

Anders, S., Pyl, P.T., and Huber, W. (2015). HTSeq--a Python framework to work with high-throughput sequencing data. Bioinformatics *31*, 166-169.

Cardona, A., Saalfeld, S., Schindelin, J., Arganda-Carreras, I., Preibisch, S., Longair, M., Tomancak, P., Hartenstein, V., and Douglas, R.J. (2012). TrakEM2 software for neural circuit reconstruction. PloS one *7*, e38011.

Dobin, A., Davis, C.A., Schlesinger, F., Drenkow, J., Zaleski, C., Jha, S., Batut, P., Chaisson, M., and Gingeras, T.R. (2013). STAR: ultrafast universal RNA-seq aligner. Bioinformatics *29*, 15-21.

Gao, S., Xie, L., Kawano, T., Po, M.D., Guan, S., Zhen, M., Pirri, J.K., and Alkema, M.J. (2015). The NCA sodium leak channel is required for persistent motor circuit activity that sustains locomotion. Nature communications *6*, 6323.

Kawano, T., Po, M.D., Gao, S., Leung, G., Ryu, W.S., and Zhen, M. (2011). An imbalancing act: gap junctions reduce the backward motor circuit activity to bias C. elegans for forward locomotion. Neuron *72*, 572-586.

Saalfeld, S., Cardona, A., Hartenstein, V., and Tomancak, P. (2009). CATMAID: collaborative annotation toolkit for massive amounts of image data. Bioinformatics *25*, 1984-1986.

Sulston, J.E., Schierenberg, E., White, J.G., and Thomson, J.N. (1983). The embryonic cell lineage of the nematode Caenorhabditis elegans. Developmental biology *100*, 64-119.

White, J.G., Southgate, E., Thomson, J.N., and Brenner, S. (1986). The structure of the nervous system of the nematode Caenorhabditis elegans. Philosophical transactions of the Royal Society of London Series B, Biological sciences *314*, 1-340.